Engineering Structures 232 (2021) 111839

Contents lists available at ScienceDirect

Engineering Structures

journal homepage: www.elsevier.com/locate/engstruct

Theoretical vehicle bridge interaction model for bridges with non-simply supported boundary conditions

Zhenhua Shi *, Nasim Uddin

Department of Civil, Construction and Environmental Engineering, The University of Alabama at Birmingham, Birmingham, AL 35294, USA

ARTICLE INFO

Keywords:
Coupled differential equation
Boundary condition
Damping
Vehicle bridge interaction
Structural dynamics

ABSTRACT

Theoretical vehicle bridge interaction (VBI) models have been widely studied for decades for the simply supported boundary condition but not for the other boundary conditions. This paper presents the mathematical models for several non-simply supported boundary conditions including both ends fixed, fixed simply supported, and one end fixed the other end free (cantilever) boundary condition. The closed-form solutions can be found under the assumption that the vehicle acceleration magnitude is far lower than the gravitational acceleration constant. The analytical solutions are then illustrated on a specific bridge example to compare the responses due to different bridge boundary conditions, and to study different vehicle parameter effects on extracting multiple bridge frequencies (five) from the vehicle responses. A signal drift phenomenon can be observed on the acceleration response of both the bridge and the vehicle, while a camel hump phenomenon can be observed on the Fast Fourier analysis of the vehicle acceleration signal. The parameter study shows that the vehicle frequency is preferred to be high due to the attenuation effect on the bridge frequencies that are higher than the vehicle frequency. The vehicle speed parameter is preferred to be low to reduce both the camel hump phenomenon and the vehicle acceleration magnitude, while both the vehicle mass and damping parameter have little effect on the multiple bridge frequencies extraction from the vehicle. Besides presenting the explicit solutions for calibrating other numerical models, this study also demonstrates the feasibility of the vehicle-based bridge health monitoring approach, as any bridge anomaly due to deterioration may be sensitively reflected on the bridge frequency list extracted from the vehicle response.

1. Introduction

Vehicle bridge interaction (VBI) is a fundamental issue in bridge engineering. Theoretically understanding the VBI mechanism is not only critical for designing a safe bridge but also beneficial for monitoring the bridge during its maintenance phase, as bridges in the transportation system are subject to a variety of issues such as aging, fatigue, creep, corrosion, uneven settlement, stress relaxation and concentration, etc. On one hand, the vehicle weight can be estimated based on the bridge response so that excessive vehicular loads in the transportation network can be monitored, this topic is more commonly known as moving force identification in literature [1–5]. On the other hand, the vehicle-based structural health monitoring of the bridges has gained wide attention due to the advantages of mobility and potential economy characteristics [6,7]. This approach assumes that the bridge dynamic information such as frequencies [8–16], mode shapes [17–22], and damping properties [23,24], can be reflected by the dynamic response of the passing vehicle, and has been widely studied both theoretically and experimentally for decades. The readers may be directed to several detailed review articles [7,25–29] about the vehicle-based structural health monitoring approach. The relevant works of this study will be briefly reviewed, with the drawbacks and problems pointed out. The novelties and significances of this study will then be stated.

The VBI problem is either studied by analytical explicit solutions [30–32] or finite element methods [33–38]. The merit of explicit solutions is that the solutions can be expressed as closed forms which may provide a theoretical reference for calibrating other methods. The closed-form solutions usually directly reveal the frequency components of both the vehicle and the bridge responses and certain features that may be expected during an experiment. In 2004, Yang et al. [8] proposed a theoretical VBI model for a simply supported boundary condition to extract the first bridge frequency from the dynamic response of a passing vehicle, in which the closed-form solutions were obtained considering only the first mode of the bridge and assuming the vehicle

* Corresponding author.
E-mail addresses: zhs@uab.edu (Z. Shi), nuddin@uab.edu (N. Uddin).

https://doi.org/10.1016/j.engstruct.2020.111839
Received 10 June 2020; Received in revised form 25 November 2020; Accepted 28 December 2020

has a mass that is an order magnitude less than the total bridge mass. Only the first bridge frequency could be identified from the vehicle since only the first bridge vibration mode was considered. Although higher bridge modes were considered in a following study [9], both the vehicle and bridge damping factors were still not considered in the mathematical model. On the other hand, the finite element method provides a way to address more complicated problems, although the solutions could not be expressed as explicit expressions. For example, to study the wheel size effect, Yang and Cao [38] recently proposed a finite element double-mass vehicle model, in which the vehicle was modelled as a sprung mass representing the vehicle body and an un-sprung disk representing the axle mass with the wheel radius. The damping effect for the suspension system was considered but not for the wheel since the commercial wheel usually consists of a rigid alloy rim and a pneumatic tire. The pneumatic tire, which is designed to provide a contact patch cushion to absorb shock and to avoid excessive bearing pressure, is believed to have significant damping contributions.

Besides theoretical studies, numerous experimental studies were also conducted to verify or explore the vehicle-based structural health monitoring techniques. In a field experimental study, Lin and Yang [10] used a truck-towed cart installed with an accelerometer to identify the first bridge frequency. Their results show that the first bridge frequency can be identified if the cart is maintained at a proper low speed (the threshold will depend on specific situation). However, the second bridge vertical (besides lateral) frequency was not identified in their tests. Wheel effect studies by Yang et al. [14] also shows that the PU (polyurethane) coated solid metal wheels performed the best for extracting bridge frequencies compared to the common commercial inflatable wheels and solid rubber wheels, since the PU wheels show no identifiable natural frequencies, while the inflatable wheels and solid rubber wheels have their own primary frequencies which may disturb the identification of the bridge frequencies. Kim and Lynch [39] used a heavy vehicle with wireless sensors to study the interaction with a continuous field steel bridge. They argued that the bridge frequencies were not identified from the heavy truck is due to possible attenuation effect of the suspension system, the reason could also be simply the pneumatic tire effect since the pneumatic tires certainly have frequency and damping property which may play a significant role in the bridge information transmission process. Cerda et al. [40] experimentally studied the vehicle-based approach for detecting different simulated damage scenarios including support rotation restrictions, adjustable damping, and adjustable mass, based on only the first bridge frequency identification results. Their study also shows low vehicle speed is beneficial for a more accurate identification result. McGetrick et al. [41] experimentally monitored the bridge stiffness using the vehicle response, when only the first frequency of the bridge can be identified. Urushadze and Yau [16] used a stiffness-adjustable vehicle to identify the frequencies of a plexiglass beam, they concluded that vehicle with a harder spring gives better predictions of the bridge frequencies. In 2017, Kim et al. [42] used a tractor-trailer vehicle to detect the bridge frequency, in which only the first bridge frequency was identified with an error of 8.8%. Those experiments show that only the first few, in some cases none, of the bridge frequencies can be detected, resulting in the necessity of reexamining the theoretical studies to identify the problems and give possible indications.

This study establishes the coupled equation group for the VBI system to include both the vehicle and bridge damping effects for bridges with several non-simply supported boundary conditions including both ends fixed, fixed simply supported, and one end fixed the other end free (cantilever) boundary condition. The closed-form solutions are sought under the assumption that the vehicle acceleration magnitude is negligible compared to the gravitational acceleration constant (g = 9.8 $m{\cdot}s^{-2}$). Due to the specialty of the mode shape expression, the most common simply supported scenario may be studied separately. Critical vehicle parameters including frequency, speed, mass, and damping are also studied based on both ends fixed scenario. This study may provide a theoretical reference for advancing the vehicle-based structural health monitoring approach of bridges, as the bridge dynamic characteristics may be timely and effectively reflected from the test vehicles. It needs to be mentioned that the road surface roughness is not considered in this study for two reasons. Firstly, the inclusion of bridge surface roughness into the equations would significantly complicate the problem and closed-form solutions may not be obtainable, the finite element method is usually adopted to address this problem. Secondly, the effect of the road profile is believed to be affected by the contact patch size of the vehicle tires. The contact patches are provided by pneumatic tires to absorb energy and to avoid excessive pressures. A large contact patch would significantly counterbalance the bridge profile to avoid separation, while a tiny contact patch may introduce jumping interaction between the vehicle and the bridge, which may require a completely different mathematical model, while this study balances the complexity of the mathematical model and the feasibility of the closed-form solutions. The obtained solutions are implemented in MATLAB [43] to graphically present the results and to study parameter effects. The Eigenfunctions of bridge natural frequencies for different boundary conditions are also solved numerically by MATLAB. This study is organized as follows: theoretical formulations for VBI with different boundary conditions are respectively introduced in Section 2; parameter baseline studies are respectively presented in Section 3 for each boundary condition; while vehicle parameter studies are presented in Section 4 based on both ends fixed boundary condition, followed by conclusions in Section 5.

2. Theoretical formulations

2.1. Equation group for general VBI

A general VBI system without boundary condition is illustrated in Fig. 1. The bridge is considered as a Bernoulli-Euler beam with uniformly distributed property including unit-length mass constant $\overline{m}$, unit-length damping constant $\overline{c}$, and section stiffnessEI, while the vehicle is simplified as a damped sprung mass with mass m_v, spring constant k_v, and damping constant c_v. A Bernoulli-Euler beam assumes that plane cross-sections remain plane during flexure. For the vehicle, the problem is to determine the response of the damped sprung mass due to support motion. It can also represent springs in parallel or series to include other factors such as multiple axle effects and tire effects. By ignoring the flexure effects caused by shear forces, rotary inertial forces, and axial forces, the equilibrium equation of the VBI system can be established as

$$\begin{cases} m_v\ddot{y}_v + c_v\left(\dot{y}_v - \dot{y}_b|_{x=vt}\right) + k_v\left(y_v - y_b|_{x=vt}\right) = 0 \\ \overline{m}\dfrac{\partial^2 y_b}{\partial t^2} + \overline{c}\dfrac{\partial y_b}{\partial t} + EI\dfrac{\partial^4 y_b}{\partial x^4} = p(x,t) \end{cases} \tag{1}$$

in which $y_v$is the vehicle displacement response which is a function of time, $y_b$is the bridge displacement response which is a function of both time and space, head dots is used for derivatives with respect to time, the

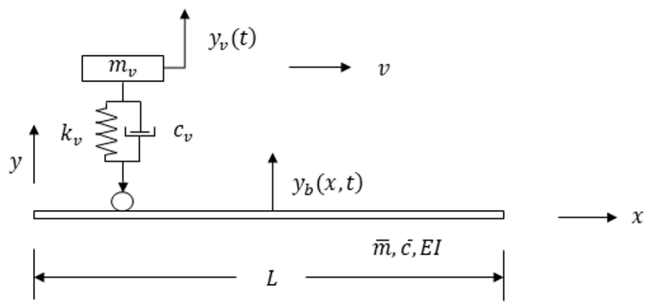

Fig. 1. General VBI model without boundary conditions.

partial differential symbol $\partial$is used for functions that have two or more variables. The lateral load distribution, $p(x,t)$ is zero everywhere along the bridge except a concentrated load at the contact point between the vehicle and the bridge, and can be described as

$$p(x,t) = \begin{cases} k_v\left(y_v - y_b|_{x=vt}\right) + c_v\left(\dot{y}_v - \dot{y}_b|_{x=vt}\right) - m_v g \\ 0 \end{cases} = \begin{cases} -m_v\ddot{y}_v - m_v g, x = vt \\ 0, x \neq vt \end{cases} \quad (2)$$

The coupled equilibrium equation group of the VBI system becomes

$$\begin{cases} m_v\ddot{y}_v + c_v\dot{y}_v + k_v y_v = k_v y_b|_{x=vt} + c_v\dot{y}_b|_{x=vt} \\ \overline{m}\dfrac{\partial^2 y_b}{\partial t^2} + \overline{c}\dfrac{\partial y_b}{\partial t} + EI\dfrac{\partial^4 y_b}{\partial x^4} = \begin{cases} -m_v(\ddot{y}_v + g), x = vt \\ 0, x \neq vt \end{cases} \end{cases} \quad (3)$$

It can be seen in the equation group that the unknown bridge response $y_b(t)$ and vehicle response $y_v(t)$ are coupled. The orthogonal nature of normal modes provides a way to address a system that has multiple degrees-of-freedom by superposition, in which the vibration of the system can be expressed in terms of a superposition of a certain number of normal modes [44]. Thus, the solution of the bridge equation can be found by the method of separation of variables, in which the solution is assumed as an infinite superposition of the products of the normal modes $\Phi_n(x)$ and time functions $z_n(t)$in the following form

$$y_b(x,t) = \sum_n \Phi_n(x) z_n(t) \quad (4)$$

Substituting into Eq. (3) would result in

$$\begin{cases} m_v\ddot{y}_v + c_v\dot{y}_v + k_v y_v = \sum_n \left[k_v z_n(t) + c_v\dot{z}_n(t)\right]\Phi_n(vt) \\ \ddot{z}_n(t) + \dfrac{\overline{c}}{\overline{m}} \end{cases} \qquad \dot{z}_n(t) + \omega_n^2 z_n(t) = \frac{\int_0^L \Phi_n(x)\begin{cases} -m_v\left(\ddot{y}_v + g\right), x = vt \\ 0, x \neq vt \end{cases} dx}{\overline{m}\int_0^L \Phi_n^2(x)dx} \quad (5)$$

in which $\overline{c}$ and $\overline{m}$are assumed as constants; while $\Phi_n(x)$ and ω_n depend on boundary conditions and have the following relationship

$$\Phi_n^{IV}(x) - \frac{\overline{m}\omega_n^2}{EI}\Phi_n(x) = 0 \quad (6)$$

Here the roman indices indicate derivatives with respect to the space variable x. The differential equation group Eq. (5) that contains the new coupled variable of$z_n(t)$and$y_v(t)$, is the exact equation group to be solved for the VBI system with both the vehicle and bridge damping effects for any boundary conditions.

2.2. Bridge with both ends fixed boundary condition

2.2.1. Bridge response

The VBI equation group in Section 2.1 applies to bridges with any boundary conditions. This section presents the bridge with both ends fixed scenario which is commonly seen on continuous bridges. Fig. 2 (a) shows a schematic of a continuous bridge span in which the boundary condition may be simplified as both ends fixed (with rotation resistance) for a theoretical VBI model as illustrated in Fig. 2 (b). When the supports deteriorate due to certain issues such as corrosion and failure in a field

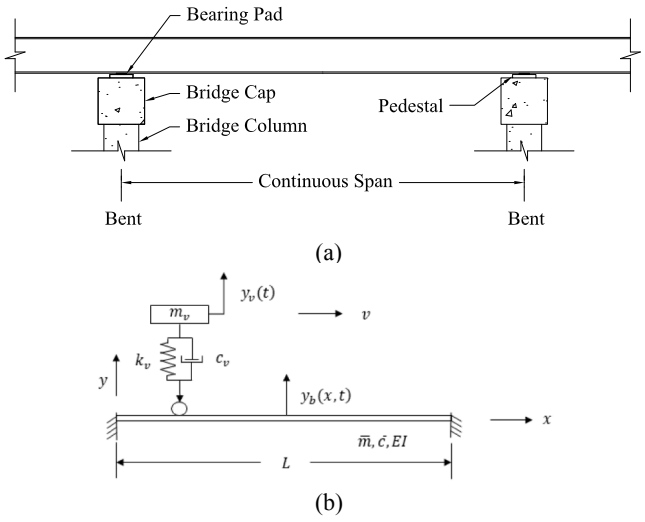

Fig. 2. Bridge with both ends fixed boundary condition (a) schematic elevation view of a bridge continuous span (b) theoretical VBI model with both ends fixed boundary condition.

bridge, the level of resistance to rotation of the support may change, which may then be reflected on the sensitive frequency list of the original bridge. For the VBI system with both ends fixed boundary condition, the normal modes are

$$\Phi_n(x) = cosa_n x - cosha_n x - \sigma_n(sina_n x - sinha_n x) \quad (7)$$

in which,

$$\sigma_n = \frac{cosa_n L - cosha_n L}{sina_n L - sinha_n L} \quad (8)$$

$$cosa_n L cosha_n L - 1 = 0 \quad (9)$$

$a_n L$ can be calculated numerically, or since the *cosh* function increases rapidly, a good approximate solution may be expressed as [45]

$$a_n L \approx \frac{(2n+1)\pi}{2} \quad (10)$$

The maximum error for the first root is 0.37% and is decreasing for higher roots, the corresponding bridge natural frequencies are

$$\omega_n = (a_n L)^2\sqrt{\frac{EI}{\overline{m}L^4}} \quad (11)$$

The equation group Eq. (5) can be decoupled if assuming$\ddot{y}_v \ll g$, in which case the equation of the bridge becomes

$$\ddot{z}_n(t) + \frac{\overline{c}}{\overline{m}}\dot{z}_n(t) + \omega_n^2 z_n(t) = -\frac{m_v g}{\overline{m}A_n}\begin{bmatrix} cosa_n vt - cosha_n vt \\ -\sigma_n(sina_n vt - sinha_n vt) \end{bmatrix} \quad (12)$$

in which,

$$A_n = \int_0^L \Phi_n^2(x)dx = \frac{1}{2a_n}\left\{\begin{array}{c} \left(\sigma_n^2-1\right)\left(e^{a_nL}-e^{-a_nL}\right)cosa_nL \\ -\left[(1-\sigma_n)^2e^{a_nL}+(1+\sigma_n)^2e^{-a_nL}\right]sina_nL \\ -\sigma_n cosh2a_nL+\dfrac{\left(1+\sigma_n^2\right)}{2}sinh2a_nL \\ +\sigma_n cos2a_nL+\dfrac{\left(1-\sigma_n^2\right)}{2}sin2a_nL+2a_nL \end{array}\right\} \tag{13}$$

Assuming zero initial conditions (bridge in the static equilibrium state), that is$z_n(0) = 0$, and $\dot{z}_n(0) = 0$, the solution to the bridge time function equation can be found as

$$z_n(t) = e^{-\xi_n\omega_n t}\left\{\begin{array}{c} A_n^* cos\left[\left(\sqrt{1-\xi_n^2}\right)\omega_n t\right] \\ +B_n^* sin\left[\left(\sqrt{1-\xi_n^2}\right)\omega_n t\right] \end{array}\right\}+\left(\begin{array}{c} C_n^* cosa_n vt+D_n^* sina_n vt \\ +G_n^* cosha_n vt+H_n^* sinha_n vt \end{array}\right) \tag{14}$$

in which,

$$\xi_n = \frac{\overline{c}}{2\overline{m}\omega_n} \tag{15}$$

and,

$$\left\{\begin{array}{c} A_n^* = -C_n^* - G_n^* \\ B_n^* = \dfrac{\xi_n\omega_n A_n^* - a_n v\left(D_n^*+H_n^*\right)}{\left(\sqrt{1-\xi_n^2}\right)\omega_n} \\ C_n^* = -\dfrac{m_v g}{\overline{m}A_n}\dfrac{\left\{\left[\omega_n^2-(a_n v)^2\right]+2\xi_n\omega_n a_n v\sigma_n\right\}}{\left[\omega_n^2-(a_n v)^2\right]^2+(2\xi_n\omega_n a_n v)^2} \\ D_n^* = -\dfrac{m_v g}{\overline{m}A_n}\dfrac{2\xi_n\omega_n a_n v-\sigma_n\left[\omega_n^2-(a_n v)^2\right]}{\left[\omega_n^2-(a_n v)^2\right]^2+(2\xi_n\omega_n a_n v)^2} \\ G_n^* = \dfrac{m_v g}{\overline{m}A_n}\dfrac{\left[\omega_n^2+(a_n v)^2\right]+2\xi_n\omega_n a_n v\sigma_n}{\left[\omega_n^2+(a_n v)^2\right]^2-(2\xi_n\omega_n a_n v)^2} \\ H_n^* = -\dfrac{m_v g}{\overline{m}A_n}\dfrac{2\xi_n\omega_n a_n v+\sigma_n\left[\omega_n^2+(a_n v)^2\right]}{\left[\omega_n^2+(a_n v)^2\right]^2-(2\xi_n\omega_n a_n v)^2} \end{array}\right. \tag{16}$$

after obtaining the time function, the displacement and acceleration response of the bridge can be respectively obtained as:

$$y_b(x,t) = \sum_n\left\{\left\{\begin{array}{c} e^{-\xi_n\omega_n t}\left\{A_n^* cos\left[\left(\sqrt{1-\xi_n^2}\right)\omega_n t\right]+B_n^* sin\left[\left(\sqrt{1-\xi_n^2}\right)\omega_n t\right]\right\} \\ +\left(C_n^* cosa_n vt+D_n^* sina_n vt+G_n^* cosha_n vt+H_n^* sinha_n vt\right) \\ \left[cosa_n x-cosha_n x-\sigma_n(sina_n x-sinha_n x)\right] \end{array}\right\}\right\} \tag{17}$$

It can be noticed that the bridge acceleration response is dominated by two different categories of frequency, the damped bridge frequencies $\left(\sqrt{1-\xi_n^2}\right)\omega_n$, and the vehicle driving frequencies $a_n v$. Due to the introduction of non-periodic hyperbolic terms, signals may be drifted.

2.2.2. Vehicle response

The bridge vibration response is transmitted to the vehicle as an input. After obtaining the time function $z_n(t)$ of the bridge, the equation for the vehicle becomes

$$\ddot{y}_v+2\xi_v\omega_v\dot{y}_v+\omega_v^2 y_v = \sum_n\left\{\left\{\begin{array}{c} e^{-\xi_n\omega_n t}\left\{\begin{array}{c} a_n^* cos\left[\left(\sqrt{1-\xi_n^2}\right)\omega_n t\right] \\ +b_n^* sin\left[\left(\sqrt{1-\xi_n^2}\right)\omega_n t\right] \end{array}\right\} \\ +c_n^* cosa_n vt+d_n^* sina_n vt \\ +g_n^* cosha_n vt+h_n^* sinha_n vt \\ \left[cosa_n vt-cosha_n vt-\sigma_n(sina_n vt-sinha_n vt)\right] \end{array}\right\}\right\} \tag{19}$$

in which

$$\ddot{y}_b(x,t) = \sum_n\left\{\left\{\begin{array}{c} e^{-\xi_n\omega_n t}\left\{\begin{array}{c} \left[\begin{array}{c}(\xi_n\omega_n)^2A_n^*-2\xi_n\omega_n\left(\sqrt{1-\xi_n^2}\right)\omega_n B_n^* \\ -\left(1-\xi_n^2\right)\omega_n^2 A_n^*\end{array}\right]cos\left[\left(\sqrt{1-\xi_n^2}\right)\omega_n t\right] \\ +\left[\begin{array}{c}(\xi_n\omega_n)^2B_n^*+2\xi_n\omega_n\left(\sqrt{1-\xi_n^2}\right)\omega_n A_n^* \\ -\left(1-\xi_n^2\right)\omega_n^2 B_n^*\end{array}\right]sin\left[\left(\sqrt{1-\xi_n^2}\right)\omega_n t\right] \end{array}\right\} \\ +(a_n v)^2\left(-C_n^* cosa_n vt-D_n^* sina_n vt\right) \\ +(a_n v)^2\left(G_n^* cosha_n vt+H_n^* sinha_n vt\right) \\ \left[cosa_n x-cosha_n x-\sigma_n(sina_n x-sinha_n x)\right] \end{array}\right\}\right\} \tag{18}$$

$$\begin{cases} a_n^* = \omega_v^2 A_n^* + 2\xi_v\omega_v\left(\sqrt{1-\xi_n^2}\right)\omega_n B_n^* - 2\xi_v\omega_v\xi_n\omega_n A_n^* \\ b_n^* = \omega_v^2 B_n^* - 2\xi_v\omega_v\left(\sqrt{1-\xi_n^2}\right)\omega_n A_n^* - 2\xi_v\omega_v\xi_n\omega_n B_n^* \\ c_n^* = \omega_v^2 C_n^* + 2\xi_v\omega_v a_n v D_n^* \\ d_n^* = \omega_v^2 D_n^* - 2\xi_v\omega_v a_n v C_n^* \\ g_n^* = \omega_v^2 G_n^* + 2\xi_v\omega_v a_n v H_n^* \\ h_n^* = \omega_v^2 H_n^* + 2\xi_v\omega_v a_n v G_n^* \end{cases} \tag{20}$$

The right-hand side expression needs to be deduced to incorporate the time-varying mode shape term$\Phi_n(vt)$. The equation of the vehicle becomes (note: for the convenience of integration, some of the hyperbolic functions were expressed by its natural exponential function forms)

$$\ddot{y}_v + 2\xi_v\omega_v\dot{y}_v + \omega_v^2 y_v =$$

The solution to this nonhomogeneous differential equation can be expressed by a complementary solution to the associated homogeneous differential equation plus a particular solution which can be obtained by solving each right-hand term and then superposing them together. The coefficients for the complementary solution can then be determined by the initial conditions (in this case, assume both the initial displacement and initial velocity of the vehicle are zero). In theory, the total response of the vehicle will then be the superposition of an infinite number of bridge vibration modes. The displacement and acceleration response are deduced respectively as:

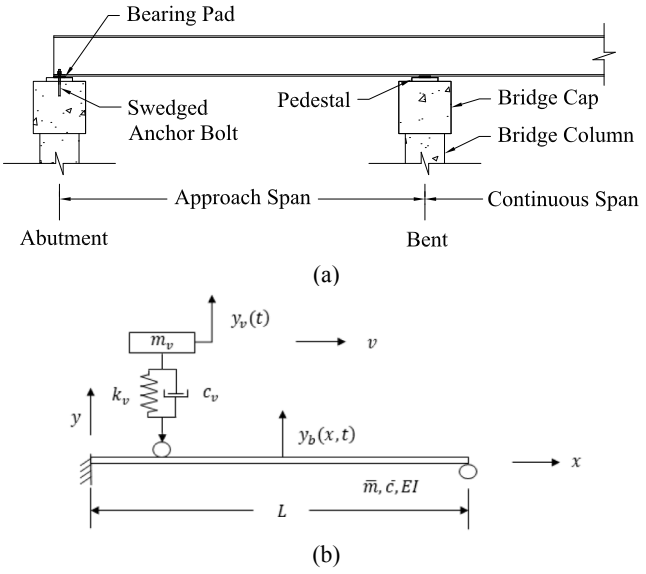

Fig. 3. Bridge with fixed simply supported boundary condition (a) schematic elevation view of a bridge approach span (b) theoretical VBI model with fixed simply supported boundary condition.

in which the detailed coefficients are summarized in the appendix. Note that the vehicle acceleration response is dominated by five different

$$\sum_n \begin{cases} +\frac{a_n^* + \sigma_n b_n^*}{2} e^{-\xi_n\omega_n t} cos\left[\left(\sqrt{1-\xi_n^2}\right)\omega_n + a_n v\right]t \\ +\frac{b_n^* - \sigma_n a_n^*}{2} e^{-\xi_n\omega_n t} sin\left[\left(\sqrt{1-\xi_n^2}\right)\omega_n + a_n v\right]t \\ +\frac{a_n^* - \sigma_n b_n^*}{2} e^{-\xi_n\omega_n t} cos\left[\left(\sqrt{1-\xi_n^2}\right)\omega_n - a_n v\right]t \\ +\frac{b_n^* + \sigma_n a_n^*}{2} e^{-\xi_n\omega_n t} sin\left[\left(\sqrt{1-\xi_n^2}\right)\omega_n - a_n v\right]t \\ +\frac{g_n^* + h_n^* + (\sigma_n - 1)c_n^*}{2} e^{a_n vt} cosa_n vt \\ +\frac{g_n^* - h_n^* - (\sigma_n + 1)c_n^*}{2} e^{-a_n vt} cosa_n vt \\ +\frac{(\sigma_n - 1)d_n^* - \sigma_n(g_n^* + h_n^*)}{2} e^{a_n vt} sina_n vt \\ -\frac{(\sigma_n + 1)d_n^* + \sigma_n(g_n^* - h_n^*)}{2} e^{-a_n vt} sina_n vt \end{cases} \begin{cases} +\frac{a_n^*(\sigma_n - 1)}{2} e^{-(\xi_n\omega_n - a_n v)t} cos\left(\sqrt{1-\xi_n^2}\right)\omega_n t \\ +\frac{b_n^*(\sigma_n - 1)}{2} e^{-(\xi_n\omega_n - a_n v)t} sin\left(\sqrt{1-\xi_n^2}\right)\omega_n t \\ -\frac{a_n^*(\sigma_n + 1)}{2} e^{-(\xi_n\omega_n + a_n v)t} cos\left(\sqrt{1-\xi_n^2}\right)\omega_n t \\ -\frac{b_n^*(\sigma_n + 1)}{2} e^{-(\xi_n\omega_n + a_n v)t} sin\left(\sqrt{1-\xi_n^2}\right)\omega_n t \\ +\frac{c_n^* + \sigma_n d_n^*}{2} cos2a_n vt + \frac{d_n^* - \sigma_n c_n^*}{2} sin2a_n vt \\ +\frac{\sigma_n h_n^* - g_n^*}{2} cosh2a_n vt + \frac{\sigma_n g_n^* - h_n^*}{2} sinh2a_n vt \\ +\frac{c_n^* - \sigma_n(d_n^* + h_n^*) - g_n^*}{2} \end{cases} \tag{21}$$

$$y_v(t)=\sum_n\left\{\begin{array}{c} e^{-\xi_v\omega_v t}\left\{M_0 cos\left[\left(\sqrt{1-\xi_v^2}\right)\omega_v t\right]+N_0 sin\left[\left(\sqrt{1-\xi_v^2}\right)\omega_v t\right]\right\} \\ +e^{-\xi_n\omega_n t}\left\{M_1 cos\left[\left(\sqrt{1-\xi_n^2}\right)\omega_n+a_n v\right]t+N_1 sin\left[\left(\sqrt{1-\xi_n^2}\right)\omega_n+a_n v\right]t\right\} \\ ++e^{-\xi_n\omega_n t}\left\{M_2 cos\left[\left(\sqrt{1-\xi_n^2}\right)\omega_n-a_n v\right]t+N_2 sin\left[\left(\sqrt{1-\xi_n^2}\right)\omega_n-a_n v\right]t\right\} \\ +e^{-(\xi_n\omega_n-a_n v)t}\left[M_3 cos\left(\sqrt{1-\xi_n^2}\right)\omega_n t+N_3 sin\left(\sqrt{1-\xi_n^2}\right)\omega_n t\right] \\ +e^{-(\xi_n\omega_n+a_n v)t}\left[M_4 cos\left(\sqrt{1-\xi_n^2}\right)\omega_n t+N_4 sin\left(\sqrt{1-\xi_n^2}\right)\omega_n t\right] \\ +e^{a_n vt}(M_5 cosa_n vt+N_5 sina_n vt)+e^{-a_n vt}(M_6 cosa_n vt+N_6 sina_n vt) \\ +M_7 cos2a_n vt+N_7 sin2a_n vt++M_8 cosh2a_n vt+N_8 sinh2a_n vt \\ +\dfrac{c_n^*-\sigma_n\left(d_n^*+h_n^*\right)-g_n^*}{2\omega_v^2} \end{array}\right\} \tag{22}$$

$$\ddot{y}_v(t)=\sum_n\left\{\begin{array}{c} e^{-\xi_v\omega_v t}\left\{m_0 cos\left[\left(\sqrt{1-\xi_v^2}\right)\omega_v t\right]+n_0 sin\left[\left(\sqrt{1-\xi_v^2}\right)\omega_v t\right]\right\} \\ +e^{-\xi_n\omega_n t}\left\{m_1 cos\left[\left(\sqrt{1-\xi_n^2}\right)\omega_n+a_n v\right]t+n_1 sin\left[\left(\sqrt{1-\xi_n^2}\right)\omega_n+a_n v\right]t\right\} \\ +e^{-\xi_n\omega_n t}\left\{m_2 cos\left[\left(\sqrt{1-\xi_n^2}\right)\omega_n-a_n v\right]t+n_2 sin\left[\left(\sqrt{1-\xi_n^2}\right)\omega_n-a_n v\right]t\right\} \\ +e^{-(\xi_n\omega_n-a_n v)t}\left[m_3 cos\left(\sqrt{1-\xi_n^2}\right)\omega_n t+n_3 sin\left(\sqrt{1-\xi_n^2}\right)\omega_n t\right] \\ +e^{-(\xi_n\omega_n+a_n v)t}\left[m_4 cos\left(\sqrt{1-\xi_n^2}\right)\omega_n t+n_4 sin\left(\sqrt{1-\xi_n^2}\right)\omega_n t\right] \\ +e^{a_n vt}(m_5 cosa_n vt+n_5 sina_n vt)+e^{-a_n vt}(m_6 cosa_n vt+n_6 sina_n vt) \\ +m_7 cos2a_n vt+n_7 sin2a_n vt+m_8 cosh2a_n vt+n_8 sinh2a_n vt \end{array}\right\} \tag{23}$$

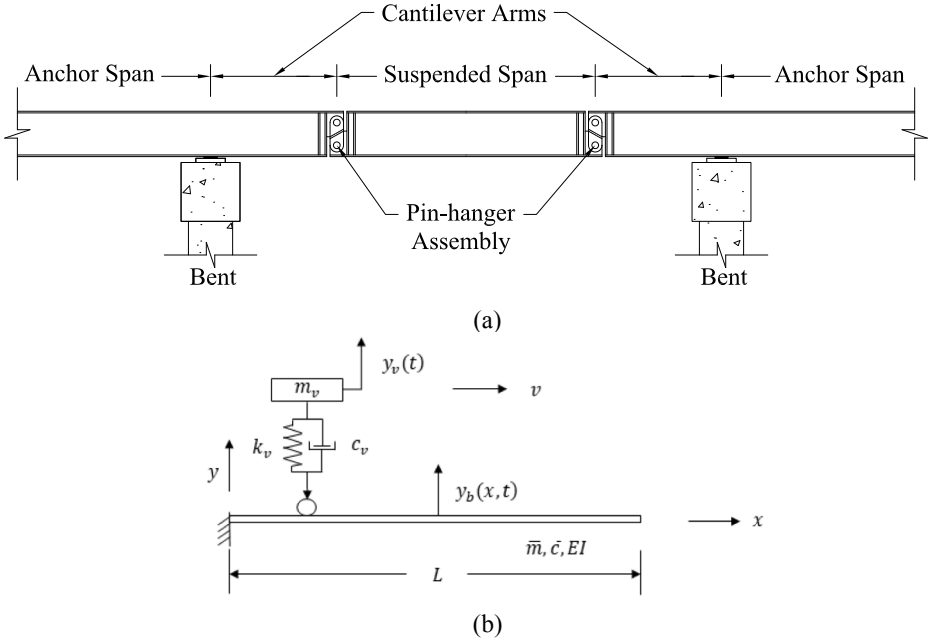

Fig. 4. Bridge with one end fixed the other end free boundary condition (a) schematic elevation view of a bridge with cantilever arms (b) theoretical VBI model with cantilever boundary condition.

Table 1
Vehicle and bridge parameters used in the analytical baseline study.

Vehicle Property		Bridge Property	
k_v(N·m^{-1})	8.0582×10^{10}	EI(N·m^2)	5.0695×10^{10}
m_v(kg)	2.2680×10^4 (40%m_b)	$\overline{m}$(kg·m^{-1})	1.8779×10^3
ξ_v	0.20	ξ_b	0.01
v(m·s^{-1})	8.94	L(m)	30.48
f_v(Hz)	300	f_b(fixed–fixed, 1st – 5th) (Hz)	19.91, 54.89, 107.62, 177.89, 265.74
		f_b(fixed-simply, 1st – 5th) (Hz)	13.72, 44.47, 92.79, 158.68, 242.13
		f_b(cantilever, 1st – 5th) (Hz)	3.13, 19.61, 54.92, 107.61, 177.89

categories of frequency due to the constrained boundary condition: the damped vehicle frequency $(\sqrt{1-\xi_v^2})\omega_v$, damped bridge frequencies $(\sqrt{1-\xi_n^2})\omega_n$, vehicle driving frequency affected damped bridge frequencies $(\sqrt{1-\xi_n^2})\omega_n \pm a_n v$, vehicle driving frequency $a_n v$, and doubled vehicle driving frequency $2a_n v$, and because of the introduction of non-periodic hyperbolic terms, signal drift may be expected.

2.3. Bridge with fixed simply supported boundary condition

Bridge with fixed simply supported boundary condition may be commonly seen on the approach spans of a continuous bridge as shown in Fig. 3 (a). The support at the abutment usually restrains the bridge end from vertical movement but not for rotational movement, while the other end is restrained for both vertical and rotational movement (to some extent due to the continuous span). Bridge span with such a kind of boundary condition may be modelled as one end fixed the other end simply supported in a theoretical VBI model as shown in Fig. 3 (b). For a field bridge, the bearing degradation may cause a simply supported condition to have some rotational resistance thus results in the original bridge to have a quite different frequency list, as bridge frequency is very sensitive to the changes of the boundary condition. For the VBI system with one end fixed the other end simply supported boundary condition, the normal modes are

$$\Phi_n(x) = cosa_n x - cosha_n x - \sigma_n(sina_n x - sinha_n x) \tag{24}$$

in which,

$$\sigma_n = \frac{cosa_n L - cosha_n L}{sina_n L - sinha_n L} \tag{25}$$

$$tana_n L = tanha_n L \tag{26}$$

in which $a_n L$can be calculated numerically, or a good approximate solution may be expressed as [45]

$$a_n L \approx \frac{(4n+1)\pi}{4} \tag{27}$$

with a decreasing error of 0.01% starting from the first mode. Since the normal mode expressions are the same as both ends fixed boundary condition, the expressions of the vehicle and bridge responses will be the same. However, $a_n$needs to be calculated differently based on new Eigen equations.

2.4. Bridge with one end fixed the other end free (cantilever) boundary condition

Bridge with one end fixed the other end free boundary condition is commonly seen on bridges with cantilever spans, suspended spans, and cantilever span systems. Fig. 4 (a) shows a schematic of a bridge with cantilever arms and a suspended span connected via a pin-hanger assembly. Those types of bridges were prevailing in the 1950s since statically determinate structures are easy to analyze, the only critical component needs to be designed is the linkage, which is the pin-hanger assembly, that supports the suspended span from the cantilevers [46]. The failure of the bridge over the Mianus River in Greenwich, Connecticut, June 1983 had such a structure system [47]. The bearing deterioration may cause the level of fixed boundary condition to be changed and thus could be reflected on the original bridge frequency list. This type of structural interaction may also be commonly seen in

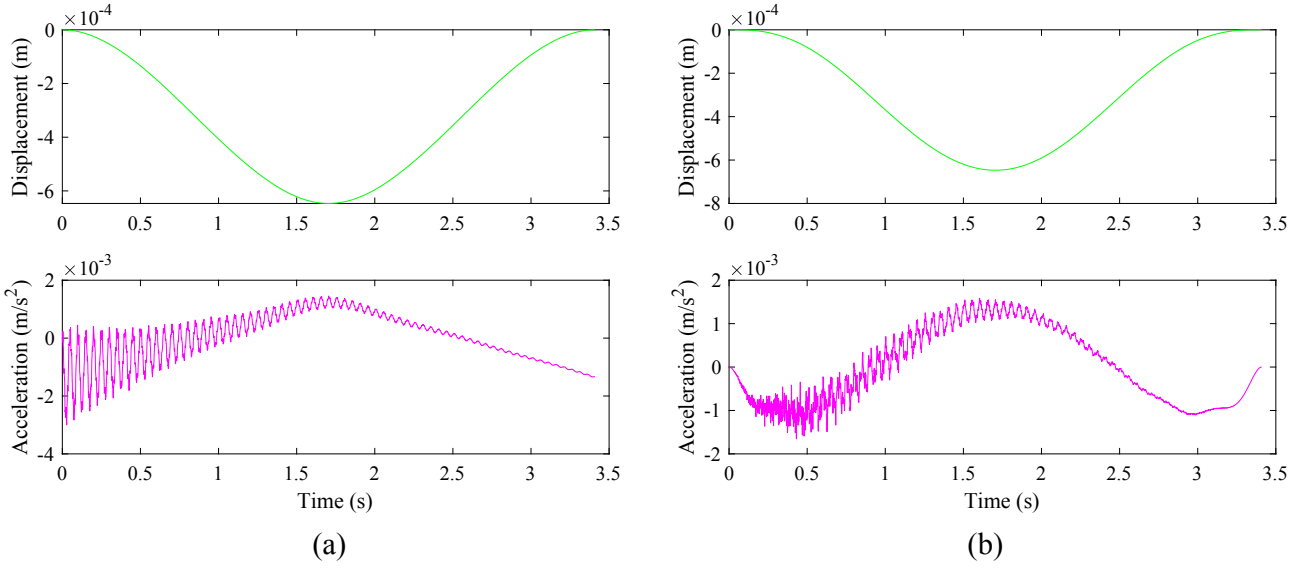

Fig. 5. Displacement and acceleration response of bridge with both ends fixed boundary condition (a) signals from the bridge middle point; (b) signals from the vehicle.

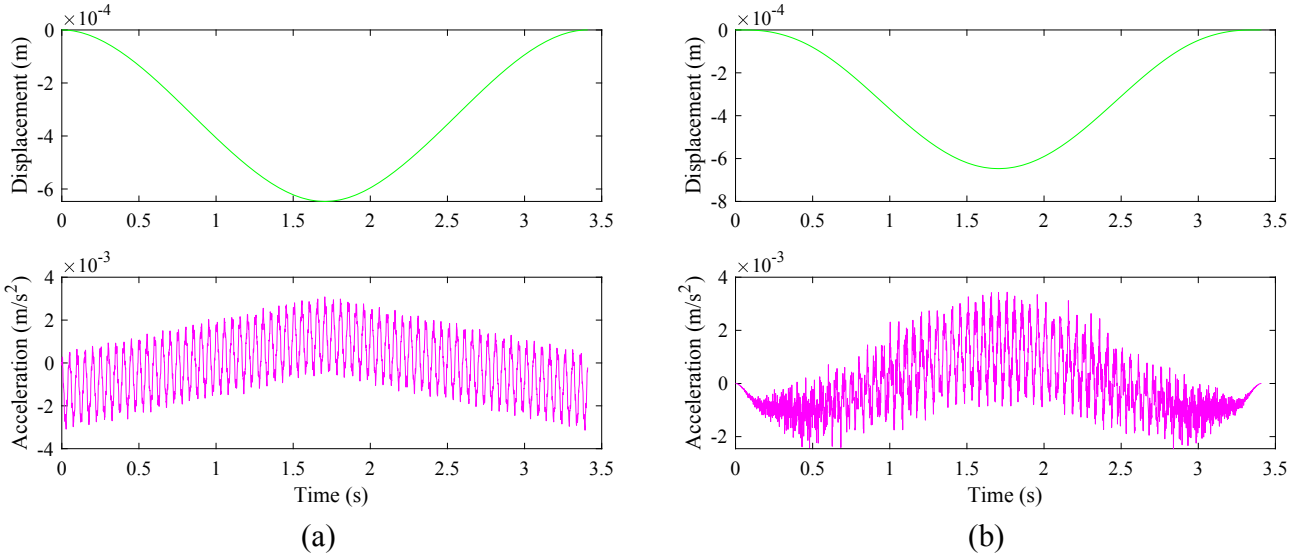

Fig. 6. Displacement and acceleration response with no damping effect ($\xi_v = 0, \xi_n = 0$) (a) signals from the bridge middle point; (b) signals from the vehicle.

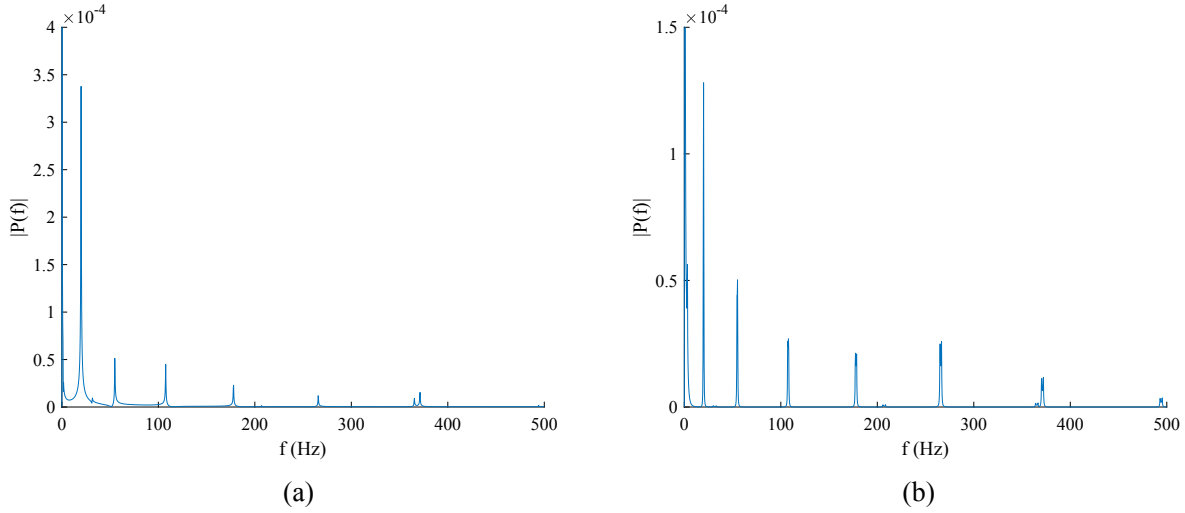

Fig. 7. Frequency analysis results of baseline parameters (a) acceleration signal from 45% of bridge length point; (b) acceleration signal from the vehicle.

Table 2
Frequency summary of VBI with both ends fixed boundary condition.

Theoretical frequency (Hz)	Signal from bridge		Signal from vehicle	
	Frequency (Hz)	Error (%)	Frequency (Hz)	Error (%)
19.91	19.94	0.15%	19.94	0.15%
54.89	54.84	0.09%	54.84	0.09%
107.62	107.60	0.02%	107.60	0.02%
177.89	178.00	0.06%	178.00	0.06%
265.74	265.70	0.02%	265.70	0.02%

Note: m_v=40%m_b, ξ_b= 0.01, ξ_v= 0.2, f_v= 300 Hz, v= 8.94 m·s^{-1}.

tower crane scenarios in construction. Structures with such a boundary condition may be mathematically represented by one end fixed and the other end free boundary condition in a theoretical VBI model as shown in Fig. 4 (b), in which the normal modes are

$$\Phi_n(x) = cosa_n x - cosha_n x - \sigma_n(sina_n x - sinha_n x) \tag{28}$$

in which,

$$\sigma_n = \frac{cosa_n L + cosha_n L}{sina_n L + sinha_n L} \tag{29}$$

$$cosa_n L cosha_n L + 1 = 0 \tag{30}$$

in which $a_n L$can be calculated numerically, or a good approximate solution except for the first mode may be expressed as [45]

$$\mathrm{a_n L} \approx \frac{(2\mathrm{n}-1)\pi}{2} \tag{31}$$

with a decreasing error of 0.39% starting from the second mode. Since the normal mode expression for this boundary condition is the same as both ends fixed scenario, the response expressions of both the vehicle and bridge will be the same, however, both $a_n$and $\sigma_n$will be calculated differently based on new expressions.

3. Parameter baseline study

A 100-ft (30.48 m) long bridge example [46] is adopted to illustrate the theoretical solutions obtained in Section 2. This example is only

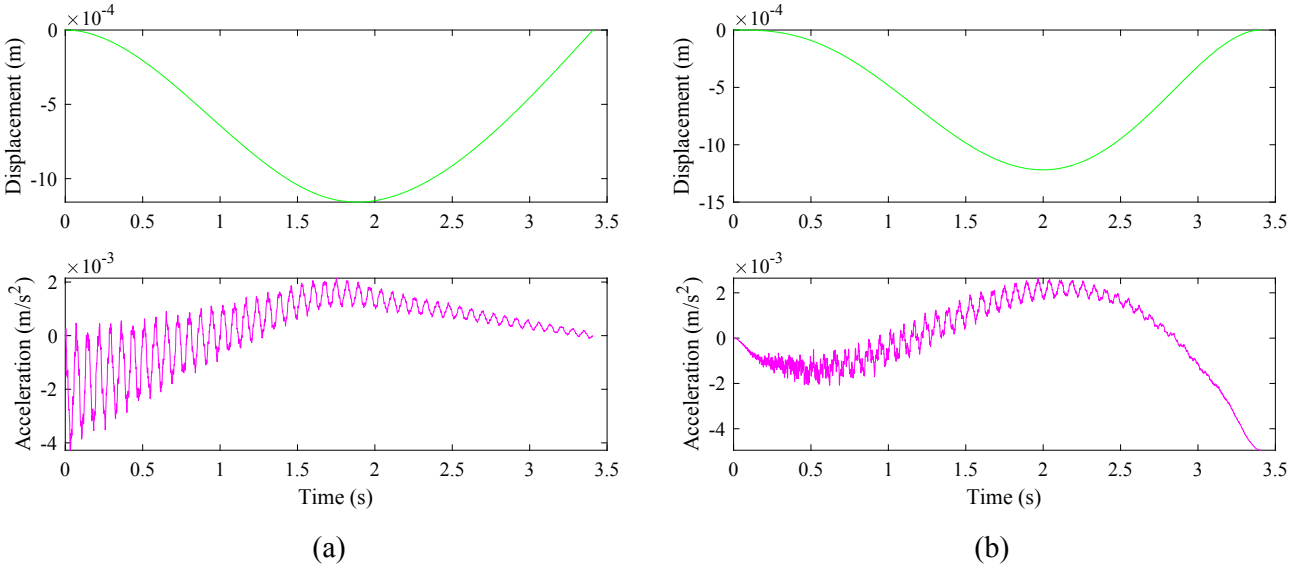

Fig. 8. Displacement and acceleration response of baseline parameters (a) signals from the bridge middle point; (b) signals from the vehicle.

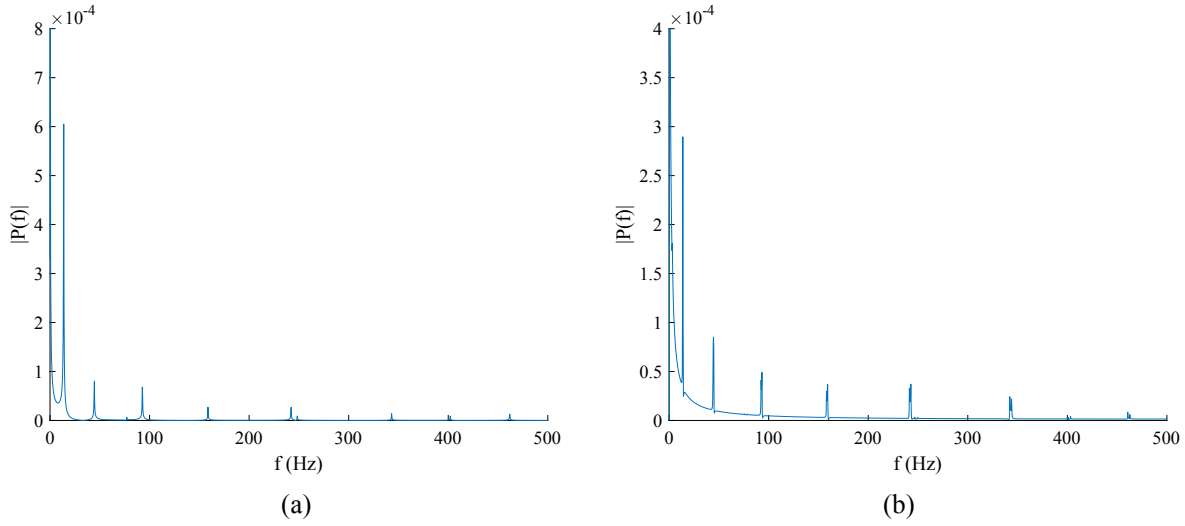

Fig. 9. Frequency analysis results of baseline parameters (a) acceleration signal from the bridge middle point; (b) acceleration signal from the vehicle.

Table 3
Frequency summary of VBI with fixed simply supported boundary condition.

Theoretical frequency (Hz)	Signal from bridge		Signal from vehicle	
	Frequency (Hz)	Error (%)	Frequency (Hz)	Error (%)
13.72	13.78	0.44%	13.78	0.44%
44.47	44.57	0.22%	44.57	0.22%
92.79	92.67	0.13%	92.67	0.13%
158.68	158.70	0.01%	158.70	0.01%
242.13	242.20	0.03%	242.20	0.03%

Note: m_v=40%m_b, ξ_b= 0.01, ξ_v= 0.2, f_v= 300 Hz, v= 8.94 m·s^{-1}.

intended to present the theoretical solutions graphically and to compare the sensitivity of bridge frequency list due to different boundary conditions, other examples could also be easily implemented into the solutions. The vehicle and bridge properties used in this illustration are summarized in Table 1. The bridge properties are equivalently calculated based on the original bridge section properties. The HL-93 (highway load, developed in 1993) design tandem load is conservatively and equivalently represented by the damped sprung mass model to the theory. The vehicle mass is initially calculated as 40% of the total bridge mass, nevertheless, vehicle mass is not directly limited in the assumption. Although the typical vehicle has low frequencies due to the suspension system and inflated tire effect, the vehicle frequency in this VBI model is initially chosen as 300 Hz to avoid the interested bridge frequencies to be extracted. A low vehicle frequency scenario of 5 Hz in the parameter study section shows that higher bridge frequencies may be more difficult to be identified from the vehicle. The vehicle stiffness is then calculated based on the mass and frequency. The vehicle speed is initially chosen as 8.94 m·s^{-1}.

Since the bridge has different damping ratios for different vibration modes, as indicated by Eq. (15), the first damping ratio is assumed for the first mode, then the unit-length damping constant $\bar{c}$ is calculated based on Eq. (15) before other damping ratios (ten modes in total) being calculated accordingly. The time step is chosen as 1×10^{-3} s, resulting in a maximum frequency identification of 500 Hz. To evaluate the frequency identification result, the frequencies of the bridge are obtained by three different approaches: theoretical values based on Eigen equations, the signal from the bridge, and the signal from the vehicle. Table 1

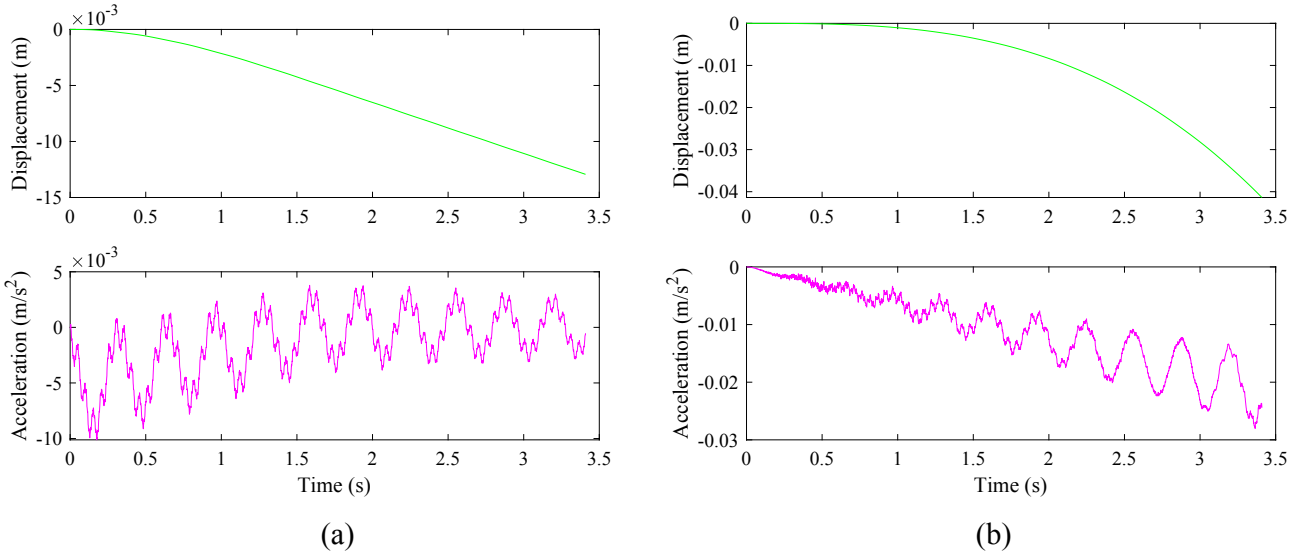

Fig. 10. Displacement and acceleration response of baseline parameters (a) signals from the bridge middle point; (b) signals from the vehicle.

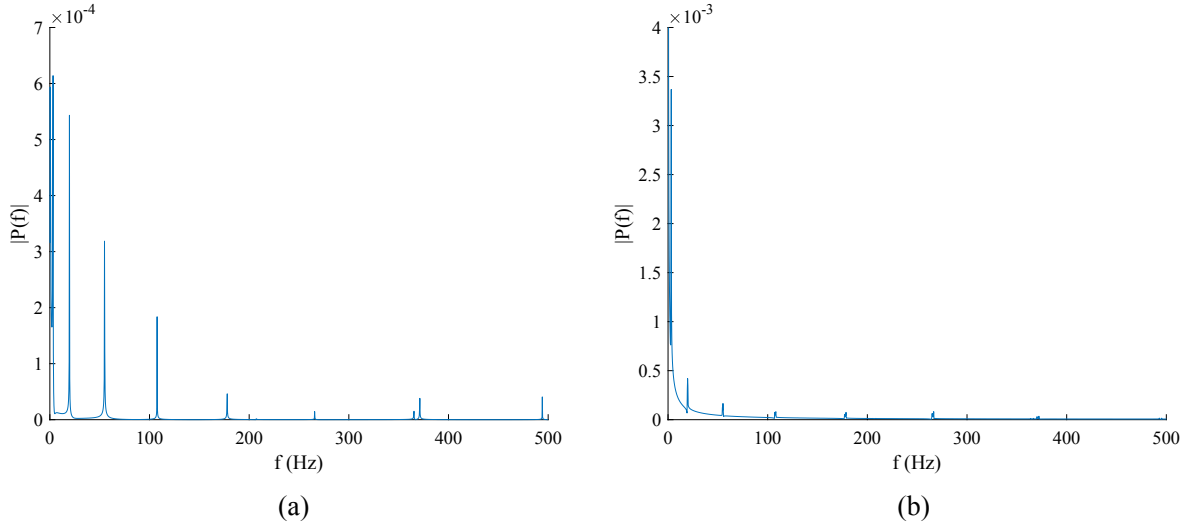

Fig. 11. Frequency analysis results of baseline parameters (a) acceleration signal from 25% of bridge length point; (b) acceleration signal from the vehicle.

Table 4
Frequency summary of VBI with one end fixed the other end free boundary condition.

Theoretical frequency (Hz)	Signal from bridge		Signal from vehicle	
	Frequency (Hz)	Error (%)	Frequency (Hz)	Error (%)
3.13	3.23	3.19%	3.23	3.19%
19.61	19.65	0.20%	19.65	0.20%
54.92	54.84	0.15%	54.84	0.15%
107.61	107.60	0.01%	107.60	0.01%
177.89	178.00	0.06%	177.70	0.11%

Note: m_v=40%m_b, ξ_b= 0.01, ξ_v= 0.2, f_v= 300 Hz, v= 8.94 m·s^{-1}.

also summarizes the first five natural frequencies of the bridge with different boundary conditions calculated based on Eigen equations to facilitate evaluating the frequency extraction results.

3.1. Bridge with both ends fixed

Fig. 5 shows the displacement and acceleration responses of the bridge middle point and the vehicle for the bridge with both ends fixed boundary condition. An interesting signal drift phenomenon can be noticed on the acceleration signal both from the bridge and the vehicle, while not on the displacement signal, although the acceleration response is simply the second time derivative of the displacement response. The drift phenomenon could be caused by the non-periodic hyperbolic terms due to the constrained boundary condition. Fig. 6 shows the results of the zero-damping scenario for both the vehicle and the bridge. The damping effect can be noticed on both the non-decay characteristic and the signal magnitude. The vehicle acceleration magnitude with the damping effect is 1.656 × 10^{-3} m·s^{-2} (0.02%g), while that of the zero damping scenario is 3.436 × 10^{-3} m·s^{-2} (0.035%g). Thus, the decoupling assumption is reasonable.

The signals from the bridge and the vehicle with damping effect are processed by Fast Fourier Transform (FFT) to obtain the frequency information, as shown in Fig. 7. Note that the bridge middle point signal may not reflect the even bridge frequencies such as the 2nd and 4th bridge frequency, the signal is instead collected at 45% of the bridge length so that the first five bridge frequencies can be reflected, the 20th bridge frequency will likely be affected since this signal location is at 9/

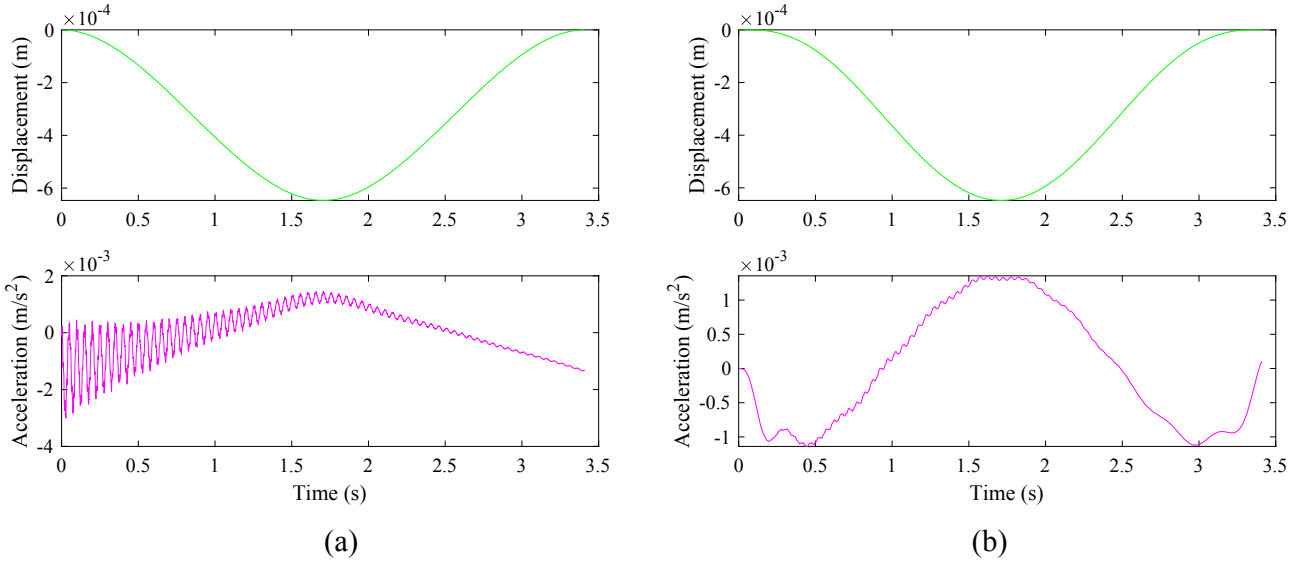

Fig. 12. Displacement and acceleration response due to vehicle frequency effect (f_v = 5 Hz) (a) signals from the bridge middle point; (b) signals from the vehicle.

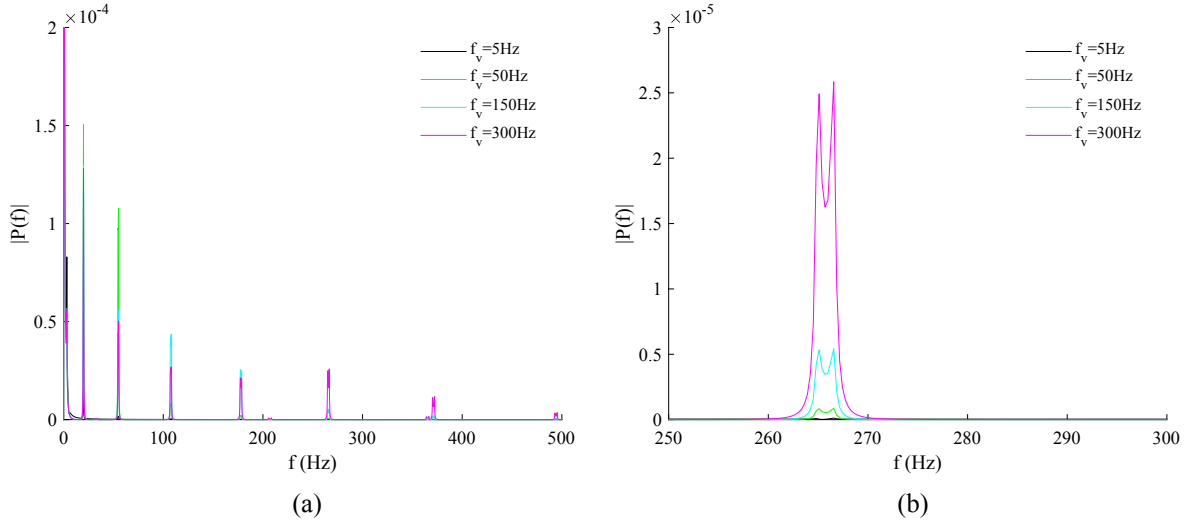

Fig. 13. FFT analysis for studying vehicle frequency effect (a) frequency range of 0–500 Hz; (b) frequency range of 250–300 Hz.

Table 5
Frequency summary of vehicle frequency effect (worst scenariof_v = 5 Hz).

Theoretical frequency (Hz)	Signal from bridge		Signal from vehicle	
	Frequency (Hz)	Error (%)	Frequency (Hz)	Error (%)
19.91	19.94	0.15%	19.94	0.15%
54.89	54.84	0.09%	54.84	0.09%
107.62	107.60	0.02%	107.60	0.02%
177.89	178.00	0.06%	177.70	0.11%
265.74	265.70	0.02%	265.40	0.13%

Note: m_v=40%m_b, ξ_b= 0.01, ξ_v= 0.2, f_v= 5 Hz, v= 8.94 m·s^{-1}

20 of the bridge length. The minor peaks in Fig. 7 may indicate other categories of frequency. A camel hump phenomenon (both left and right bridge frequency shift) can be seen on the higher bridge frequencies ($\geq 3^{rd}$ in this example) when identifying frequency from the FFT result of the vehicle signal, as shown in Fig. 7(b). The camel hump phenomenon is due to the term $\left(\sqrt{1-\xi_n^2}\right)\omega_n \pm a_n v$, and can be noticed more clearly for high bridge frequencies and high vehicle speeds. The frequency analysis result is summarized in Table 2, note that due to the camel hump phenomenon, the frequencies identified from vehicle signal are read at the trough point of each camel hump. The result is almost the same for the signals from the bridge itself and the vehicle, with an excellent error of less than 0.15% compared to the theoretical values.

3.2. *Bridge with fixed simply supported boundary condition*

This section briefly presents the VBI result for the bridge with fixed simply supported boundary condition. Fig. 8 shows the displacement and acceleration response for the bridge middle point and the vehicle, while Fig. 9 shows the FFT result of the acceleration signals. Note that the bridge middle point signal is selected since the mode shape is not symmetric due to asymmetric boundary condition. The theoretical assumption is reasonable since the vehicle acceleration magnitude is 4.948 × 10^{-3} m·s^{-2} (0.05%g). Compared to both ends fixed boundary condition which shows a symmetric bell-shape displacement response, the simply supported boundary condition shows a non-symmetric displacement response both for the bridge and for the vehicle. Consistent with both ends fixed boundary condition, the acceleration signals

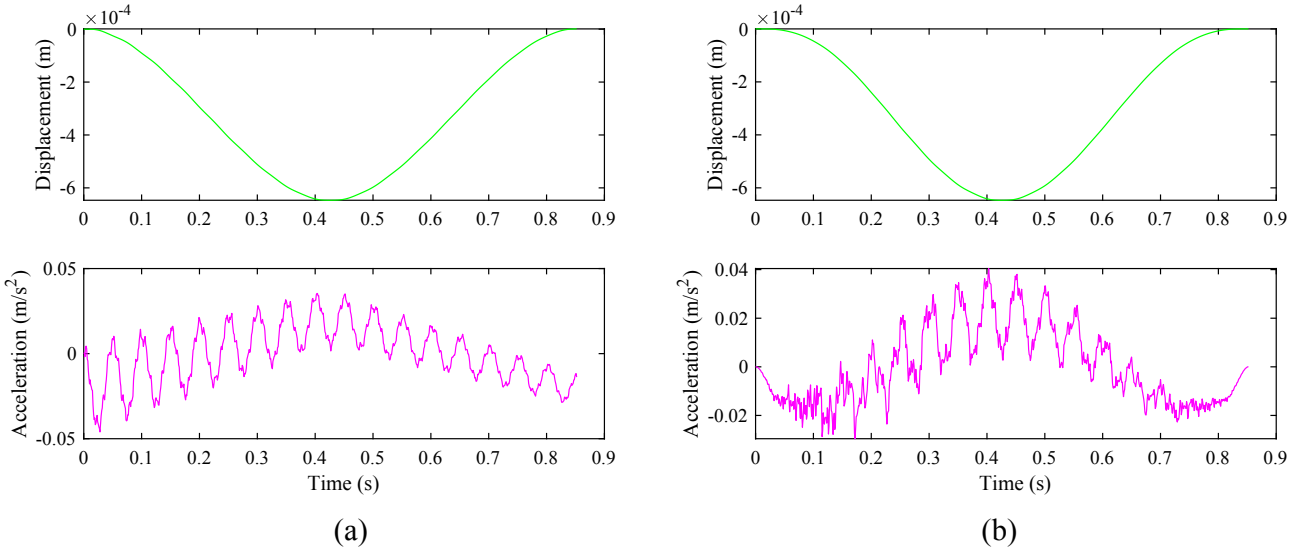

Fig. 14. Displacement and acceleration response due to vehicle speed effect ($v = 35.76$ m·s^{-1}) (a) signals from the bridge middle point; (b) signals from the vehicle.

Table 6
Frequency summary of vehicle speed effect (worst scenario$v = 35.76$ m·s^{-1}).

Theoretical frequency (Hz)	Signal from bridge		Signal from vehicle	
	Frequency (Hz)	Error (%)	Frequency (Hz)	Error (%)
19.91	19.93	0.10%	19.93	0.10%
54.89	55.10	0.38%	55.10	0.38%
107.62	107.90	0.26%	106.70	0.85%
177.89	178.20	0.17%	179.40	0.85%
265.74	266.10	0.14%	264.90	0.32%

Note: m_v=40%m_b, ξ_b= 0.01, ξ_v= 0.2, f_v= 300 Hz, v= 35.76 m·s^{-1}.

for the fixed simply supported boundary condition also show drift phenomenon. Frequency analysis shows an excellent error of 0.44%, as summarized in Table 3.

3.3. Bridge with one end fixed the other end free (cantilever) boundary condition

This section briefly presents the VBI result for the bridge with one end fixed the other end free boundary condition. Fig. 10 shows the displacement and acceleration response for the bridge middle point and the vehicle. An acceleration signal drift can be noticed due to the cantilever boundary condition. The theoretical assumption is reasonable since the acceleration magnitude from the vehicle is 2.803 × 10^{-2} m·s^{-2} (0.29%g). Fig. 11 shows the FFT result of the acceleration signals, which indicates in field application, the frequency may be more difficult to be identified. Note that the signal at 25% of the bridge length is chosen to obtain the information of the first five bridge frequencies. The frequency identification result shows an increased error of 3.19%, as summarized in Table 4.

4. Vehicle parameter effect

Based on both ends fixed boundary condition, this section presents the effect of several vehicle parameters including frequency, speed, mass and damping on multiple bridge frequencies extraction from the vehicle response. Both the bridge middle point and vehicle responses are presented for the worst scenario of each vehicle parameter. The vehicle frequency plays a significant role in attenuating higher bridge frequencies and is preferred to be beyond the interested bridge frequency

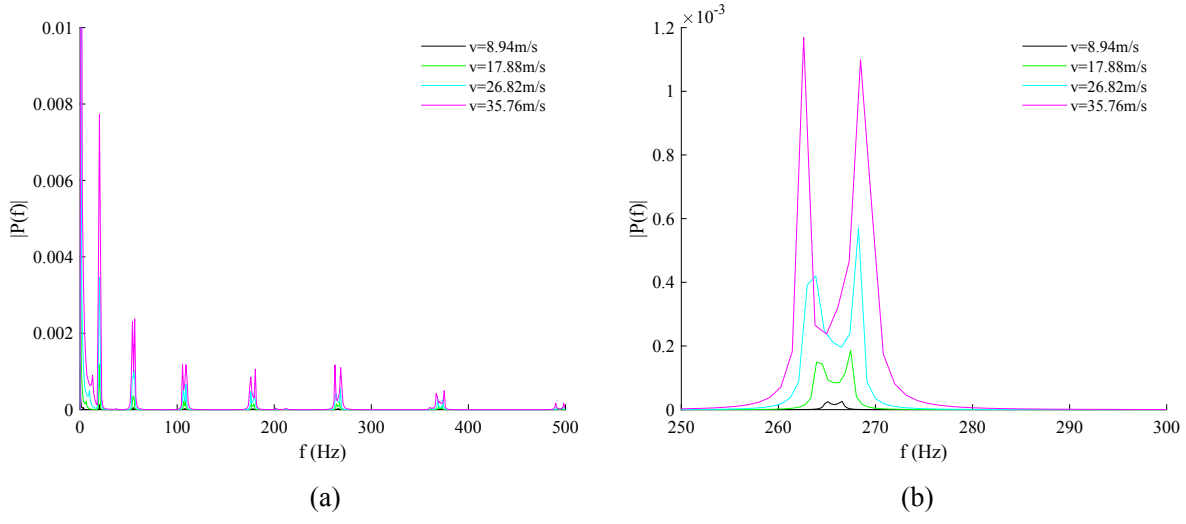

Fig. 15. FFT analysis for studying vehicle speed effect (a) frequency range 0–500 Hz; (b) frequency range 250–300 Hz.

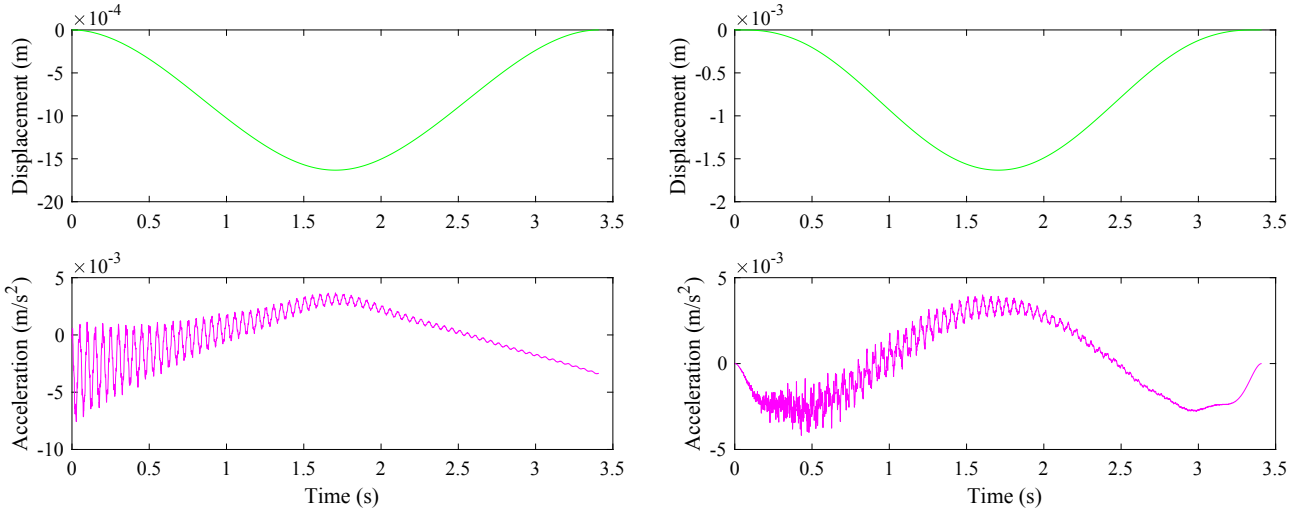

Fig. 16. Displacement and acceleration response due to vehicle mass effect (vehicle mass is 100% of the total bridge mass) (a) signals from the bridge middle point; (b) signals from the vehicle.

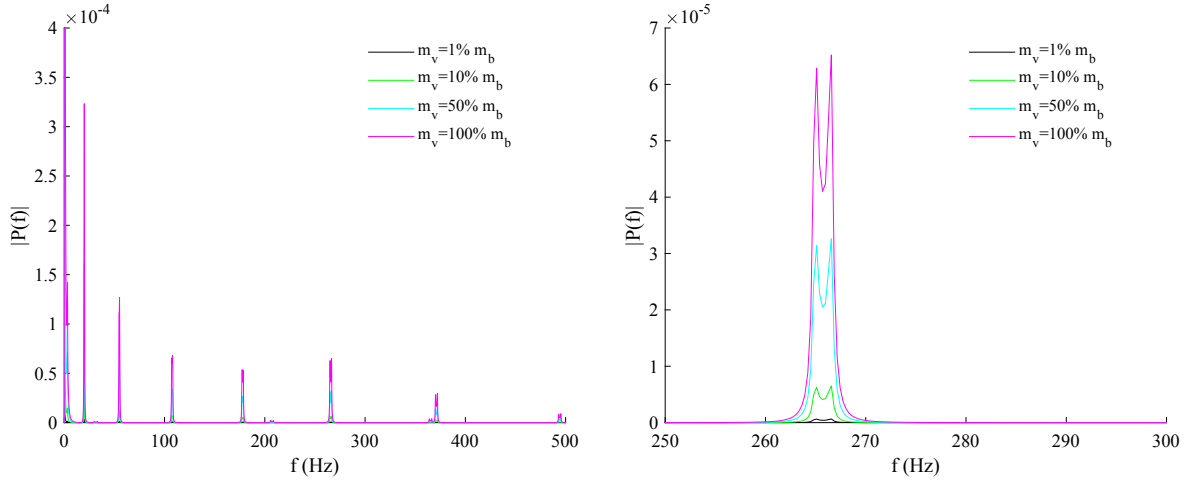

Fig. 17. Frequency analysis for studying vehicle mass effect (a) frequency range 0–500 Hz; (b) frequency range 250–300 Hz.

Table 7
Frequency summary of vehicle mass effect (worst scenario $m_v = 100\%.m_b$).

Theoretical frequency (Hz)	Signal from bridge		Signal from vehicle	
	Frequency (Hz)	Error (%)	Frequency (Hz)	Error (%)
19.91	19.94	0.15%	19.94	0.15%
54.89	54.84	0.09%	55.13	0.44%
107.62	107.60	0.02%	107.60	0.02%
177.89	178.00	0.06%	178.00	0.06%
265.74	265.70	0.02%	265.70	0.02%

Note: m_v=100%m_b, ξ_b= 0.01, ξ_v= 0.2, f_v= 300 Hz, v=8.94 m·s^{-1}.

range. Vehicle speed is preferred to be low since higher vehicle speed intensifies the camel hump phenomenon and the vehicle acceleration magnitude. Vehicle mass is not significantly limited in this theory due to the constrained boundary condition, as vehicle as heavy as the total bridge mass travelling at a high speed (35.76 m·s^{-1}) could still meet the assumption. Vehicle damping has little effect on extracting multiple bridge frequencies information. Detailed results and discussions of each parameter are presented in the following sections.

4.1. Vehicle frequency effect

This section demonstrates that the vehicle frequency plays a significant role in transmitting multiple bridge frequencies. Vehicle frequency scenarios including 5 Hz, 50 Hz, 150 Hz, and 300 Hz are selected to study the effect. Fig. 12 shows respectively the responses of the bridge at its middle point and the vehicle for the 5 Hz scenario. The assumption is reasonable since the acceleration magnitude from the vehicle is 1.355 × 10^{-3} m·s^{-2} (0.014%g). The FFT analysis for all frequency scenarios is shown in Fig. 13, in which the 5th bridge frequency is focused to give a clearer result. The attenuation effect of the vehicle with low frequency can be seen for higher bridge frequencies, although the maximum frequency identification error, as summarized in Table 5, is still as low as the baseline study. The attenuation effect is that the power spectral density (PSD) drops to 0.8% from the 1st mode to the 5th mode for the vehicle frequency of 5 Hz, while that drops to 12.7% for the vehicle frequency of 300 Hz. Severer attenuation effect will certainly affect the identification of higher bridge frequencies. The indication here is that the test vehicle may be preferred to be designed with a high frequency beyond the interested bridge frequency range for field application.

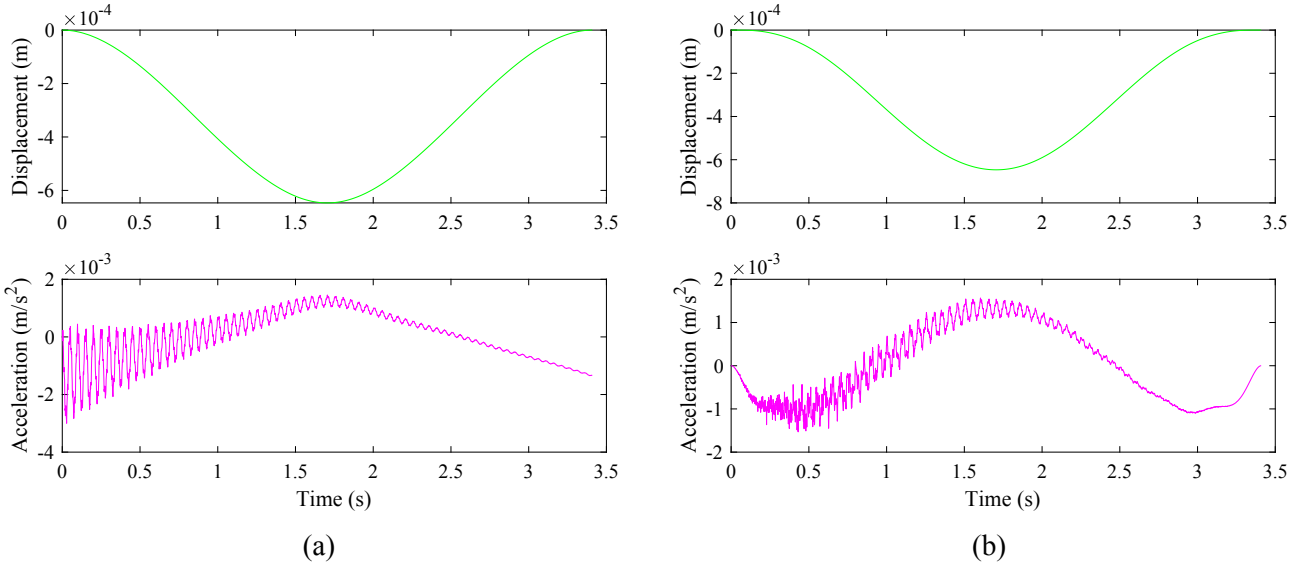

Fig. 18. Displacement and acceleration response due to vehicle damping effect ($\xi_v = 0.5$) (a) signals from the bridge middle point; (b) signals from the vehicle.

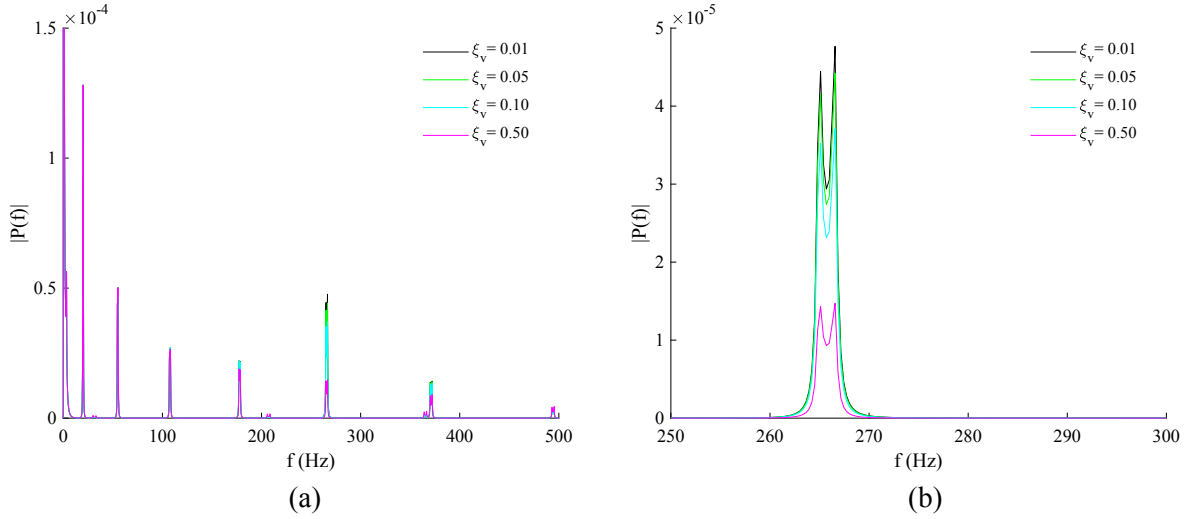

Fig. 19. FFT analysis for studying vehicle damping effect (a) frequency range 0–500 Hz; (b) frequency range 250–300 Hz.

Table 8
Frequency summary of vehicle damping effect (worst scenario $\xi_v = 0.5$).

Theoretical frequency (Hz)	Signal from bridge		Signal from vehicle	
	Frequency (Hz)	Error (%)	Frequency (Hz)	Error (%)
19.91	19.94	0.15%	19.94	0.15%
54.89	54.84	0.09%	55.13	0.44%
107.62	107.60	0.02%	107.60	0.02%
177.89	178.00	0.06%	178.00	0.06%
265.74	265.70	0.02%	265.70	0.02%

Note: m_v=40%m_b, ξ_b= 0.01, ξ_v= 0.5, f_v= 300 Hz, v= 8.94 m·s^{-1}.

4.2. Vehicle speed effect

A sequential of the vehicle speed of 8.94 m·s^{-1}, 17.88 m·s^{-1}, 26.82 m·s^{-1}, and 35.76 m·s^{-1} are selected to study the vehicle speed effect. Fig. 14 shows the displacement and acceleration response for the bridge middle point and the vehicle for the highest speed scenario (35.76 m·s^{-1}). The maximum vehicle acceleration magnitude is 4.043 × 10^{-2} m·s^{-2} (0.41%g), indicating the assumption is still reasonable. The frequencies are identified at the trough point of each camel hump and are summarized in Table 6. Due to the increased vehicle speed, the maximum frequency identification error for the bridge and vehicle is increased to 0.38% and 0.85%, respectively. The FFT result as shown in Fig. 15 shows that the camel hump phenomenon is intensified as the vehicle speed increases. The camel hump phenomenon may adversely affect the bridge frequency identification in field application, as bridges in the field often involve noise caused by many other sources such as ambient vibration, traffic, and road surface roughness. Higher vehicle speed also shows severer attenuation effect, as the PSD drops to 12.7% and 3.1% from the 1st mode to the 5th mode for the vehicle speed of 8.94 m·s^{-1} and 35.76 m·s^{-1}, respectively.

An interesting field study in literature [14] shows that as the vehicle speed increases from 2 km·h^{-1} (0.56 m·s^{-1}) to 4 km·h^{-1} (1.11 m·s^{-1}) and then 8 km·h^{-1} (2.22 m·s^{-1}), the acceleration magnitude increases roughly from 50 Gal (0.5 m·s^{-2}) to 100 Gal (1 m·s^{-2}) and then 200 Gal (2 m·s^{-2}). Their FFT frequency study also shows that the bridge frequencies are getting more ambiguous as the vehicle speed increases. The explanation could be that the vehicle acceleration signal magnitude is

too high to meet theoretical assumption, as 200 Gal (2 m·s^{-2}) is already 20.4%g. The indication here is that to extract multiple bridge frequencies, the vehicle acceleration magnitude should be maintained far lower than the gravitational acceleration constant.

4.3. Vehicle mass effect

A set of vehicle mass of 1%, 10%, 50%, and 100% of the total bridge mass are selected to study the vehicle mass effect. The vehicle mass linearly affects the vehicle acceleration magnitude which may challenge the assumption. The maximum vehicle acceleration magnitude is 4.179 $\times$ 10^{-3} m·s^{-2} (0.04%g), as presented in Fig. 16, indicating the assumption is reasonable. Fig. 17 shows the FFT analysis for all vehicle mass scenarios, the vehicle mass parameter shows no attenuation effect on the PSD, as the PSD drops to 12.7% from the 1st mode to the 5th mode for both the lowest and highest vehicle mass scenarios. Table 7 summarizes the frequency identification results for the highest vehicle mass scenario, which shows that the maximum frequency identification error is as low as the baseline scenario.

4.4. Vehicle damping effect

This section briefly presents the vehicle damping effect. Vehicle damping ratios including 0.01, 0.05, 0.1, and 0.5 are selected to study the effect. Fig. 18 show the displacement and acceleration response for the bridge middle point and the vehicle for the highest vehicle damping ratio of 0.5. The FFT analysis for all damping ratio scenarios is shown in Fig. 19. Higher vehicle damping ratio decreases PSD, as the PSD drops to 22.9% and 7.3% from the 1st mode to the 5th mode for the vehicle damping ratio of 0.01 and 0.5, respectively. The vehicle damping also has a slight effect on the vehicle acceleration magnitude. As the vehicle damping increases, the vehicle acceleration magnitude decreases from 1.841 $\times$ 10^{-3} m·s^{-2} (0.019%g) to 1.569 $\times$ 10^{-3} m·s^{-2} (0.016%g). Table 8 summarizes the frequency identification results for the highest vehicle damping ratio, which shows that vehicle damping has little effect on extracting multiple bridge frequencies from the vehicle.

5. Conclusions

The coupled differential equation group for the vehicle bridge interaction model including both the vehicle and bridge damping effects is established for the bridge with both ends fixed, fixed simply supported, and one end fixed the other end free (cantilever) boundary condition. The vehicle is theoretically modelled as a damped sprung mass, rather than only a sprung mass, to account for both the frequency and damping property of the vehicle. The assumption to decouple the equation group requires that the vehicle acceleration magnitude should be far lower than the gravitational acceleration constant. The closed-form solutions indicate that five different categories of frequency may be expected from the vehicle signal, and more categories of frequency may be expected for more comprehensive models and field applications. Conclusions drawn regarding the theoretical study as well as the parameter study include:

1) The theoretical study shows that multiple bridge frequencies can be identified from the vehicle with high accuracy (both ends fixed: 0.15%, fixed simply: 0.44%, cantilever: 3.19%), and since the bridge frequency list is very sensitive to its boundary conditions, bridge boundary condition deterioration such as bearing degradation would be highly reflected on the original bridge frequency list evolution and thus could be monitored.
2) Although the vehicle frequency parameter study shows a maximum vehicle acceleration magnitude of 0.014%g and a maximum frequency identification error of 0.15%, vehicle frequency plays a significant role in naturally attenuating higher bridge frequencies and therefore vehicle frequency is preferred to be designed higher than the interested bridge frequencies to be extracted. The attenuation effect of the vehicle frequency parameter is that the PSD drops to 0.8% and 12.7% from the 1st mode to the 5th mode for the vehicle frequency of 5 Hz and 300 Hz, respectively.
3) The vehicle speed parameter study shows a maximum vehicle acceleration magnitude of 0.41%g and a maximum frequency identification error of 0.85%, indicating that the vehicle speed is not significantly limited in this theoretical model. However, high vehicle speed results in more evident camel hump phenomenon which would broaden the bridge frequency peaks and adversely disturb multiple bridge frequencies identification from the vehicle. Higher vehicle speed also shows severer attenuation effect, as the PSD drops to 12.7% and 3.1% from the 1st mode to the 5th mode for the vehicle speed of 8.94 m·s^{-1} and 35.76 m·s^{-1}, respectively.
4) Although the vehicle mass linearly affects the vehicle acceleration magnitude, the maximum vehicle acceleration magnitude is only 0.04%g and the maximum frequency identification error is 0.44%, indicating that vehicle mass has little effect on multiple bridge frequencies identification from the vehicle. The vehicle mass parameter also shows no attenuation effect on the PSD of the frequency analysis.
5) The vehicle damping parameter study shows a maximum vehicle acceleration magnitude of 0.019%g and a maximum frequency identification error of 0.44%, indicating that the vehicle damping has little effect on multiple bridge frequencies extraction from the vehicle. Higher vehicle damping ratio yet shows more evident attenuation effect, as the PSD drops to 22.9% and 7.3% from the 1st mode to the 5th mode for the vehicle damping ratio of 0.01 and 0.5, respectively.

CRediT authorship contribution statement

Zhenhua Shi: Conceptualization, Methodology, Software, Validation, Formal analysis, Investigation, Resources, Data curation, Writing - original draft, Writing - review & editing, Visualization. **Nasim Uddin:** Conceptualization, Resources, Writing - review & editing, Supervision, Project administration, Funding acquisition.

Declaration of Competing Interest

The authors declare that they have no known competing financial interests or personal relationships that could have appeared to influence the work reported in this paper.

Acknowledgement

The authors would like to express their gratitude to the financial support received from the National Science Foundation [grant numbers NSF-CNS-1645863, NSF-CSR-1813949]. The funding sources had no other roles during this study.

Appendix

Coefficients of vehicle displacement and acceleration response for VBI model with both ends fixed boundary condition:

$$\begin{cases} m_0 = (\xi_v\omega_v)^2 M_0 - 2\xi_v\omega_v N_0\left(\sqrt{1-\xi_v^2}\right)\omega_v - M_0\left(1-\xi_v^2\right)\omega_v^2 \\ n_0 = (\xi_v\omega_v)^2 N_0 + 2\xi_v\omega_v M_0\left(\sqrt{1-\xi_v^2}\right)\omega_v - N_0\left(1-\xi_v^2\right)\omega_v^2 \end{cases} \tag{A.1}$$

$$\begin{cases} m_1 = (\xi_n\omega_n)^2 M_1 - 2\xi_n\omega_n N_1\left[\left(\sqrt{1-\xi_n^2}\right)\omega_n + a_n v\right] - M_1\left[\left(\sqrt{1-\xi_n^2}\right)\omega_n + a_n v\right]^2 \\ n_1 = (\xi_n\omega_n)^2 N_1 + 2\xi_n\omega_n M_1\left[\left(\sqrt{1-\xi_n^2}\right)\omega_n + a_n v\right] - N_1\left[\left(\sqrt{1-\xi_n^2}\right)\omega_n + a_n v\right]^2 \end{cases} \tag{A.2}$$

$$\begin{cases} m_2 = (\xi_n\omega_n)^2 M_2 - 2\xi_n\omega_n N_2\left[\left(\sqrt{1-\xi_n^2}\right)\omega_n - a_n v\right] - M_2\left[\left(\sqrt{1-\xi_n^2}\right)\omega_n - a_n v\right]^2 \\ n_2 = (\xi_n\omega_n)^2 N_2 + 2\xi_n\omega_n M_2\left[\left(\sqrt{1-\xi_n^2}\right)\omega_n - a_n v\right] - N_2\left[\left(\sqrt{1-\xi_n^2}\right)\omega_n - a_n v\right]^2 \end{cases} \tag{A.3}$$

$$\begin{cases} m_3 = (\xi_n\omega_n - a_n v)^2 M_3 - 2(\xi_n\omega_n - a_n v)N_3\left(\sqrt{1-\xi_n^2}\right)\omega_n - M_3\left(1-\xi_n^2\right)\omega_n^2 \\ n_3 = (\xi_n\omega_n - a_n v)^2 N_3 + 2(\xi_n\omega_n - a_n v)M_3\left(\sqrt{1-\xi_n^2}\right)\omega_n - N_3\left(1-\xi_n^2\right)\omega_n^2 \end{cases} \tag{A.4}$$

$$\begin{cases} m_4 = (\xi_n\omega_n + a_n v)^2 M_4 - 2(\xi_n\omega_n + a_n v)N_4\left(\sqrt{1-\xi_n^2}\right)\omega_n - M_4\left(1-\xi_n^2\right)\omega_n^2 \\ n_4 = (\xi_n\omega_n + a_n v)^2 N_4 + 2(\xi_n\omega_n + a_n v)M_4\left(\sqrt{1-\xi_n^2}\right)\omega_n - N_4\left(1-\xi_n^2\right)\omega_n^2 \end{cases} \tag{A.5}$$

$$\begin{cases} m_5 = 2(a_n v)^2 N_5 \\ n_5 = -2(a_n v)^2 M_5 \end{cases} \tag{A.6}$$

$$\begin{cases} m_6 = -2(a_n v)^2 N_6 \\ n_6 = 2(a_n v)^2 M_6 \end{cases} \tag{A.7}$$

$$\begin{cases} m_7 = -(2a_n v)^2 M_7 \\ n_7 = -(2a_n v)^2 N_7 \end{cases} \tag{A.8}$$

$$\begin{cases} m_8 = (2a_n v)^2 M_8 \\ n_8 = (2a_n v)^2 N_8 \end{cases} \tag{A.9}$$

$$M_0 = -\frac{c_n^* - \sigma_n\left(d_n^* + h_n^*\right) - g_n^*}{2\omega_v^2} - \sum_{i=1}^{8} M_i \tag{A.10}$$

$$N_0 = \frac{1}{\left(\sqrt{1-\xi_v^2}\right)\omega_v}\left[\xi_v\omega_v M_0 + \xi_n\omega_n\sum_{i=1}^{4} M_i - \left(\sqrt{1-\xi_n^2}\right)\omega_n\sum_{i=1}^{4} N_i - a_n v\begin{pmatrix} M_3 - M_4 + M_5 - M_6 \\ +N_1 - N_2 + N_5 + N_6 \\ +2N_7 + 2N_8 \end{pmatrix}\right] \tag{A.11}$$

$$\begin{cases} M_1 = \dfrac{a_n^* + \sigma_n b_n^*}{2} C_1 - \dfrac{b_n^* - \sigma_n a_n^*}{2} D_1 \\ N_1 = \dfrac{a_n^* + \sigma_n b_n^*}{2} D_1 + \dfrac{b_n^* - \sigma_n a_n^*}{2} C_1 \end{cases} \tag{A.12}$$

$$\begin{cases} M_2 = \dfrac{a_n^* - \sigma_n b_n^*}{2} C_2 - \dfrac{b_n^* + \sigma_n a_n^*}{2} D_2 \\ N_2 = \dfrac{a_n^* - \sigma_n b_n^*}{2} D_2 + \dfrac{b_n^* + \sigma_n a_n^*}{2} C_2 \end{cases} \tag{A.13}$$

$$\begin{cases} M_3 = \dfrac{a_n^*(\sigma_n - 1)}{2} C_3 - \dfrac{b_n^*(\sigma_n - 1)}{2} D_3 \\ N_3 = \dfrac{a_n^*(\sigma_n - 1)}{2} D_3 + \dfrac{b_n^*(\sigma_n - 1)}{2} C_3 \end{cases} \tag{A.14}$$

$$\begin{cases} M_4 = -\dfrac{a_n^*(\sigma_n + 1)}{2} C_4 + \dfrac{b_n^*(\sigma_n + 1)}{2} D_4 \\ N_4 = -\dfrac{a_n^*(\sigma_n + 1)}{2} D_4 - \dfrac{b_n^*(\sigma_n + 1)}{2} C_4 \end{cases} \tag{A.15}$$

$$\begin{cases} M_5 = \dfrac{g_n^* + h_n^* + (\sigma_n - 1)c_n^*}{2} C_5 - \dfrac{(\sigma_n - 1)d_n^* - \sigma_n(g_n^* + h_n^*)}{2} D_5 \\ N_5 = \dfrac{g_n^* + h_n^* + (\sigma_n - 1)c_n^*}{2} D_5 + \dfrac{(\sigma_n - 1)d_n^* - \sigma_n(g_n^* + h_n^*)}{2} C_5 \end{cases} \tag{A.16}$$

$$\begin{cases} M_6 = \dfrac{g_n^* - h_n^* - (\sigma_n + 1)c_n^*}{2} C_6 + \dfrac{(\sigma_n + 1)d_n^* + \sigma_n(g_n^* - h_n^*)}{2} D_6 \\ N_6 = \dfrac{g_n^* - h_n^* - (\sigma_n + 1)c_n^*}{2} D_6 - \dfrac{(\sigma_n + 1)d_n^* + \sigma_n(g_n^* - h_n^*)}{2} C_6 \end{cases} \tag{A.17}$$

$$\begin{cases} M_7 = \dfrac{c_n^* + \sigma_n d_n^*}{2} C_{13} - \dfrac{d_n^* - \sigma_n c_n^*}{2} D_{13} \\ N_7 = \dfrac{c_n^* + \sigma_n d_n^*}{2} D_{13} + \dfrac{d_n^* - \sigma_n c_n^*}{2} C_{13} \end{cases} \tag{A.18}$$

$$\begin{cases} M_8 = \dfrac{\sigma_n h_n^* - g_n^*}{2} C_{15} + \dfrac{\sigma_n g_n^* - h_n^*}{2} D_{15} \\ N_8 = \dfrac{\sigma_n h_n^* - g_n^*}{2} D_{15} + \dfrac{\sigma_n g_n^* - h_n^*}{2} C_{15} \end{cases} \tag{A.19}$$

$$\begin{cases} C_1 = \dfrac{(\xi_n\omega_n)^2 - \left[\left(\sqrt{1-\xi_n^2}\right)\omega_n + a_n v\right]^2 - 2\xi_v\omega_v\xi_n\omega_n + \omega_v^2}{\left\{(\xi_n\omega_n)^2 - \left[\left(\sqrt{1-\xi_n^2}\right)\omega_n + a_n v\right]^2 - 2\xi_v\omega_v\xi_n\omega_n + \omega_v^2\right\}^2 + \left\{2(\xi_v\omega_v - \xi_n\omega_n)\left[\left(\sqrt{1-\xi_n^2}\right)\omega_n + a_n v\right]\right\}^2} \\ D_1 = \dfrac{2(\xi_v\omega_v - \xi_n\omega_n)\left[\left(\sqrt{1-\xi_n^2}\right)\omega_n + a_n v\right]}{\left\{(\xi_n\omega_n)^2 - \left[\left(\sqrt{1-\xi_n^2}\right)\omega_n + a_n v\right]^2 - 2\xi_v\omega_v\xi_n\omega_n + \omega_v^2\right\}^2 + \left\{2(\xi_v\omega_v - \xi_n\omega_n)\left[\left(\sqrt{1-\xi_n^2}\right)\omega_n + a_n v\right]\right\}^2} \end{cases} \tag{A.20}$$

$$\begin{cases} C_2 = \dfrac{(\xi_n\omega_n)^2 - \left[\left(\sqrt{1-\xi_n^2}\right)\omega_n - a_n v\right]^2 - 2\xi_v\omega_v\xi_n\omega_n + \omega_v^2}{\left\{(\xi_n\omega_n)^2 - \left[\left(\sqrt{1-\xi_n^2}\right)\omega_n - a_n v\right]^2 - 2\xi_v\omega_v\xi_n\omega_n + \omega_v^2\right\}^2 + \left\{2(\xi_v\omega_v - \xi_n\omega_n)\left[\left(\sqrt{1-\xi_n^2}\right)\omega_n - a_n v\right]\right\}^2} \\ D_2 = \dfrac{2(\xi_v\omega_v - \xi_n\omega_n)\left[\left(\sqrt{1-\xi_n^2}\right)\omega_n - a_n v\right]}{\left\{(\xi_n\omega_n)^2 - \left[\left(\sqrt{1-\xi_n^2}\right)\omega_n - a_n v\right]^2 - 2\xi_v\omega_v\xi_n\omega_n + \omega_v^2\right\}^2 + \left\{2(\xi_v\omega_v - \xi_n\omega_n)\left[\left(\sqrt{1-\xi_n^2}\right)\omega_n - a_n v\right]\right\}^2} \end{cases} \tag{A.21}$$

$$\begin{cases} C_3 = \dfrac{(\xi_n\omega_n - a_n v)^2 - \left(1-\xi_n^2\right)\omega_n^2 - 2\xi_v\omega_v(\xi_n\omega_n - a_n v) + \omega_v^2}{\left\{(\xi_n\omega_n - a_n v)^2 - \left(1-\xi_n^2\right)\omega_n^2 - 2\xi_v\omega_v(\xi_n\omega_n - a_n v) + \omega_v^2\right\}^2 + \left\{2(\xi_v\omega_v - (\xi_n\omega_n - a_n v))\left(\sqrt{1-\xi_n^2}\right)\omega_n\right\}^2} \\ D_3 = \dfrac{2(\xi_v\omega_v - (\xi_n\omega_n - a_n v))\left(\sqrt{1-\xi_n^2}\right)\omega_n}{\left\{(\xi_n\omega_n - a_n v)^2 - \left(1-\xi_n^2\right)\omega_n^2 - 2\xi_v\omega_v(\xi_n\omega_n - a_n v) + \omega_v^2\right\}^2 + \left\{2(\xi_v\omega_v - (\xi_n\omega_n - a_n v))\left(\sqrt{1-\xi_n^2}\right)\omega_n\right\}^2} \end{cases} \tag{A.22}$$

$$\begin{cases} C_4 = \dfrac{(\xi_n\omega_n + a_n v)^2 - \left(1-\xi_n^2\right)\omega_n^2 - 2\xi_v\omega_v(\xi_n\omega_n + a_n v) + \omega_v^2}{\left\{(\xi_n\omega_n + a_n v)^2 - \left(1-\xi_n^2\right)\omega_n^2 - 2\xi_v\omega_v(\xi_n\omega_n + a_n v) + \omega_v^2\right\}^2 + \left\{2(\xi_v\omega_v - (\xi_n\omega_n + a_n v))\left(\sqrt{1-\xi_n^2}\right)\omega_n\right\}^2} \\ D_4 = \dfrac{2(\xi_v\omega_v - (\xi_n\omega_n + a_n v))\left(\sqrt{1-\xi_n^2}\right)\omega_n}{\left\{(\xi_n\omega_n + a_n v)^2 - \left(1-\xi_n^2\right)\omega_n^2 - 2\xi_v\omega_v(\xi_n\omega_n + a_n v) + \omega_v^2\right\}^2 + \left\{2(\xi_v\omega_v - (\xi_n\omega_n + a_n v))\left(\sqrt{1-\xi_n^2}\right)\omega_n\right\}^2} \end{cases} \tag{A.23}$$

$$\begin{cases} C_5 = \dfrac{2\xi_v\omega_v a_n v + \omega_v^2}{\left\{2\xi_v\omega_v a_n v + \omega_v^2\right\}^2 + \left\{2(\xi_v\omega_v + a_n v)a_n v\right\}^2} \\ D_5 = \dfrac{2(\xi_v\omega_v + a_n v)a_n v}{\left\{2\xi_v\omega_v a_n v + \omega_v^2\right\}^2 + \left\{2(\xi_v\omega_v + a_n v)a_n v\right\}^2} \end{cases} \tag{A.24}$$

$$\begin{cases} C_6 = \dfrac{-2\xi_v\omega_v a_n v + \omega_v^2}{\left\{-2\xi_v\omega_v a_n v + \omega_v^2\right\}^2 + \left\{2(\xi_v\omega_v - a_n v)a_n v\right\}^2} \\ D_6 = \dfrac{2(\xi_v\omega_v - a_n v)a_n v}{\left\{-2\xi_v\omega_v a_n v + \omega_v^2\right\}^2 + \left\{2(\xi_v\omega_v - a_n v)a_n v\right\}^2} \end{cases} \tag{A.25}$$

$$\begin{cases} C_{13} = \dfrac{\omega_v^2 - (2a_n v)^2}{\left[\omega_v^2 - (2a_n v)^2\right]^2 + (4\xi_v\omega_v a_n v)^2} \\ D_{13} = \dfrac{4\xi_v\omega_v a_n v}{\left[\omega_v^2 - (2a_n v)^2\right]^2 + (4\xi_v\omega_v a_n v)^2} \end{cases} \tag{A.26}$$

$$\begin{cases} C_{15} = \dfrac{\omega_v^2 + (2a_n v)^2}{\left[(2a_n v)^2 + \omega_v^2\right]^2 - (4\xi_v\omega_v a_n v)^2} \\ D_{15} = -\dfrac{4\xi_v\omega_v a_n v}{\left[(2a_n v)^2 + \omega_v^2\right]^2 - (4\xi_v\omega_v a_n v)^2} \end{cases} \tag{A.27}$$

References

[1] Law SS, Chan THT, Zeng QH. Moving force identification: a time domain method. J Sound Vib 1997;201(1):1–22. https://doi.org/10.1006/jsvi.1996.0774.

[2] Chan THT, Yu L, Law SS, Yung TH. Moving force identification studies, I: theory. J Sound Vib 2001;247(1):59–76. https://doi.org/10.1006/jsvi.2001.3630.

[3] Chan THT, Ashebo DB. Theoretical study of moving force identification on continuous bridges. J Sound Vib 2006;295(3–5):870–83. https://doi.org/10.1016/j.jsv.2006.01.059.

[4] Cantero D, González A. Bridge damage detection using weigh-in-motion technology. J Bridge Eng 2015;20(5):04014078. https://doi.org/10.1061/(asce)be.1943-5592.0000674.

[5] Obrien EJ, Fitzgerald PC, Malekjafarian A, Sevillano E. Bridge damage detection using vehicle axle-force information. Eng Struct 2017;153 71. https://doi.org/10.1016/j.engstruct.2017.10.012.

[6] Malekjafarian A, McGetrick PJ, Obrien EJ. A review of indirect bridge monitoring using passing vehicles. Shock Vib 2015. https://doi.org/10.1155/2015/286139.

[7] Yang YB, Yang JP. State-of-the-art review on modal identification and damage detection of bridges by moving test vehicles. Int J Struct Stab Dy 2018;18(02):1850025. https://doi.org/10.1142/s0219455418500256.

[8] Yang YB, Lin CW, Yau JD. Extracting bridge frequencies from the dynamic response of a passing vehicle. J Sound Vib 2004:471–93. https://doi.org/10.1016/s0022-460x(03)00378-x.

[9] Yang YB, Lin CW. Vehicle–bridge interaction dynamics and potential applications. J Sound Vib 2005;284(1–2):205–26. https://doi.org/10.1016/j.jsv.2004.06.032.

[10] Lin CW, Yang YB. Use of a passing vehicle to scan the fundamental bridge frequencies: an experimental verification. Eng Struct 2005;27(13):1865–78. https://doi.org/10.1016/j.engstruct.2005.06.016.

[11] McGetrick PJ, Gonzlez A, Obrien EJ. Theoretical investigation of the use of a moving vehicle to identify bridge dynamic parameters. Insight-Non-Destruct Test Condit Monit 2009;51(8):433–8. https://doi.org/10.1784/insi.2009.51.8.433.

[12] Yang YB, Chang KC. Extraction of bridge frequencies from the dynamic response of a passing vehicle enhanced by the EMD technique. J Sound Vib 2009:718–39. https://doi.org/10.1016/j.jsv.2008.11.028.

[13] Yang YB, Chang KC. Extracting the bridge frequencies indirectly from a passing vehicle: parametric study. Eng Struct 2009;31(10):2448–59. https://doi.org/10.1016/j.engstruct.2009.06.001.

[14] Yang YB, Chen WF, Yu HW, Chan CS. Experimental study of a hand-drawn cart for measuring the bridge. Eng Struct 2013:222–31. https://doi.org/10.1016/j.engstruct.2013.09.007.

[15] Yang YB, Chen WF. Extraction of bridge frequencies from a moving test vehicle by stochastic subspace identification. J Bridge Eng 2016;21(3):04015053. https://doi.org/10.1061/(asce)be.1943-5592.0000792.

[16] Urushadze S, Yau JD. Experimental verification of indirect bridge frequency measurement using a passing vehicle. Procedia Eng 2017;190:554–9. https://doi.org/10.1016/j.proeng.2017.05.379.

[17] Yang YB, Li YC, Chang KC. Constructing the mode shapes of a bridge from a passing vehicle: a theoretical study. Smart Struct Syst 2014;13(5):797–819. https://doi.org/10.12989/sss.2014.13.5.797.

[18] Malekjafarian A, Obrien EJ. Identification of bridge mode shapes using short time frequency domain decomposition of the responses measured in a passing vehicle. Eng Struct 2014;81:386–97. https://doi.org/10.1016/j.engstruct.2014.10.007.

[19] OBrien EJ, Malekjafarian A. A mode shape-based damage detection approach using laser measurement from a vehicle crossing a simply supported bridge. Struct Control Hlth 2016;23(10):1273–86. https://doi.org/10.1002/stc.1841.

[20] Malekjafarian A, Obrien EJ. On the use of a passing vehicle for the estimation of bridge mode shapes. J Sound Vib 2017;397:77–91. https://doi.org/10.1016/j.jsv.2017.02.051.

[21] Qi ZQ, Au FTK. Identifying mode shapes of girder bridges using dynamic responses extracted from a moving vehicle under impact excitation. Int J Struct Stab Dy 2017;17(08):1750081. https://doi.org/10.1142/s021945541750081x.

[22] Yang YB, Zhang B, Qian Y, Wu Y. Contact-point response for modal identification of bridges by a moving test vehicle. Int J Struct Stab Dy 2018;1850073. https://doi.org/10.1142/s0219455418500736.

[23] González A, OBrien EJ, McGetrick PJ. Identification of damping in a bridge using a moving instrumented vehicle. J Sound Vib 2012;331(18):4115–31. https://doi.org/10.1016/j.jsv.2012.04.019.

[24] Keenahan J, OBrien EJ, McGetrick PJ, Gonzalez A. The use of a dynamic truck–trailer drive-by system to monitor bridge damping. Struct Health Monit 2014;13(2):143–57. https://doi.org/10.1177/1475921713513974.

[25] Zhu XQ, Law SS. Structural health monitoring based on vehicle-bridge interaction: accomplishments and challenges. Adv Struct Eng 2015;18(12):1999–2015. https://doi.org/10.1260/1369-4332.18.12.1999.

[26] Zhang Y, Wang L, Zhao H, Lie ST. Extraction of mode shapes of beam-like structures from the dynamic response of a moving mass. Acta Mech Sin 2019;35(3):664–73. https://doi.org/10.1007/s10409-018-0831-7.

[27] Malekjafarian A, McGetrick PJ, OBrien EJ. A review of indirect bridge monitoring using passing vehicles. Shock Vib 2015;2015:1–16. https://doi.org/10.1155/2015/286139.

[28] Yang YB, Yang JP, Zhang B, and Wu Y. Vehicle scanning method for bridges. London: John Wiley and Sons, Ltd.; 2019. https://doi.org/10.1002/9781119539629.

[29] Shokravi H, Shokravi H, Bakhary N, Heidarrezaei M, Rahimian Koloor SS, Petrů M. Vehicle-assisted techniques for health monitoring of bridges. Sensors 2020;20(12):3460.

[30] Yang YB, Li YC, Chang KC. Effect of road surface roughness on the response of a moving vehicle for identification of bridge frequencies. Interact Multiscale Mech 2012;5(4):347–68. https://doi.org/10.12989/imm.2012.5.4.347.

[31] Yang YB, Cheng MC, Chang KC. Frequency variation in vehicle-bridge interaction systems. Int J Struct Stab Dyn 2013;13(02):1350019.

[32] He WY, Zhu S. Moving load-induced response of damaged beam and its application in damage localization. J Vib Control 2016;22(16):3601–17. https://doi.org/10.1177/1077546314564587.

[33] Yang YB, Lin BH. Vehicle-bridge interaction analysis by dynamic condensation method. J Struct Eng 1995;121(11):1636–43. https://doi.org/10.1061/(asce)0733-9445(1995)121:11(1636).

[34] Bu JQ, Law SS, Zhu XQ. Innovative bridge condition assessment from dynamic response of a passing vehicle. J Eng Mech 2006;132(12):1372–9. https://doi.org/10.1061/(asce)0733-9399(2006)132:12(1372).

[35] Nasrellah HA, Manohar CS. A particle filtering approach for structural system identification in vehicle–structure interaction problems. J Sound Vib 2010;329(9):1289–309. https://doi.org/10.1016/j.jsv.2009.10.041.

[36] Rocha JM, Henriques AA, Calçada R. Probabilistic assessment of the train running safety on a short-span high-speed railway bridge. Struct Infrastruct Eng 2015;12(1):78–92. https://doi.org/10.1080/15732479.2014.995106.

[37] Greco F, Lonetti P, Pascuzzo A. A moving mesh FE methodology for vehicle–bridge interaction modeling. Mech Adv Mater Struct 2018;27(14):1256–68. https://doi:10.1080/15376494.2018.1506955.

[38] Yang JP, Cao CY. Wheel size embedded two-mass vehicle model for scanning bridge frequencies. Acta Mech 2020;231(4):1461–75. https://doi.org/10.1007/s00707-019-02595-5.

[39] Kim J, Lynch JP. Experimental analysis of vehicle–bridge interaction using a wireless monitoring system and a two-stage system identification technique. Mech Syst. Signal Pr 2012;28:3–19. https://doi.org/10.1016/j.ymssp.2011.12.008.
[40] Cerda F, Chen S, Bielak J, Garrett JH, Rizzo P, Kovačević J. Indirect structural health monitoring of a simplified laboratory-scale bridge model. Smart Struct. Syst. 2014;13(5):849–68. https://doi.org/10.12989/sss.2014.13.5.849.
[41] McGetrick PJ, Kim CW, González A, Obrien EJ. Experimental validation of a drive-by stiffness identification method for bridge monitoring. Struct. Health Monit. 2015;14(4):317–31. https://doi.org/10.1177/1475921715578314.
[42] Kim CW, Chang KC, McGetrick J, Inoue S, Hasegawa S. Utilizing moving vehicles as sensors for bridge condition screening-a laboratory verification. Sensor Mater 2017;29(2):153–63. https://doi.org/10.18494/sam.2017.1433.
[43] MATLAB, Version R2019a (9.6.0.1072779). The MathWorks Inc., Natick, Massachusetts; 2019.
[44] Paz M, Leigh W. Structural dynamics: theory and computation. 5th ed. New York: Springer Science & Business Media Inc.; 2004.
[45] Rao SS. Vibration of continuous systems. John Wiley & Sons; 2007. https://doi.org/10.1007/978-1-4612-4036-5_4.
[46] Barker RM, Puckett JA. Design of highway bridges: An LRFD approach. John Wiley & Sons; 2013. https://doi.org/10.1002/9781118411124.
[47] NTSB. Collapse of a Suspended Span of Interstate Route 95 Highway Bridge over the Mianus River, Greenwich, Connecticut, June 28, 1983. Highway Accident Report No. NTSBHAR-84/03. National Transportation Safety Board, Washington, DC.